The Dual Nature of Entrainment-Mixing Signatures Revealed through Large-Eddy Simulations of a Convection-Cloud Chamber

AARON WANG,[a] MIKHAIL OVCHINNIKOV,[a] FAN YANG,[b] WILL CANTRELL,[c] JAEMIN YEOM,[c] AND RAYMOND A. SHAW[c]

[a] *Pacific Northwest National Laboratory, Richland, Washington*
[b] *Brookhaven National Laboratory, Upton, New York*
[c] *Michigan Technological University, Houghton, Michigan*

(Manuscript received 6 March 2024, in final form 25 June 2024, accepted 20 September 2024)

ABSTRACT: Entrainment of subsaturated air into a cloud can influence its optical and microphysical properties in various ways, depending on the droplet evaporation and turbulent mixing time scales. Previous experiments in the Pi convection-cloud chamber have revealed that, given a fixed entrained air property, the mixing of entrained subsaturated air results in complete evaporation of some cloud droplets, with the rest remaining unchanged. This is a signature of inhomogeneous mixing. While comparing the results of entrainment with varying air properties, the mixing signature appears as if the subsaturated air is well mixed with the cloud to evenly reduce the droplets' size. In other words, taken together, the experiments appear to have the signature of homogeneous mixing. To explore these results in a greater depth, we conduct large-eddy simulations combined with a bin microphysics scheme. Our results reproduce the similar signatures of inhomogeneous and homogeneous mixing, implying that LES can resolve the inhomogeneous mixing when the grid spacing is smaller than the entrained air parcel. Additionally, we observe that increasing the aerosol injection rate enhances the signature of inhomogeneous mixing, while coarser grid spacing diminishes it. Finally, the change in wall fluxes in response to various entrained air properties confirms that the homogeneous signature seen in the analysis of an ensemble of simulations is the result of various equilibrium states. This further strengthens the suggestion that the homogeneous mixing signature found in aircraft observations near the cloud top may result from combining entrainment events of different intensities, possibly caused by various-sized eddies.

SIGNIFICANCE STATEMENT: Large-eddy simulation and size-resolved microphysics can resolve time scales for turbulent mixing and evaporation and, therefore, are well suited for reproducing, extending, and interpreting the entrainment experiment in the Pi convection-cloud chamber. Our simulation results confirm (i) the inhomogeneous mixing signature for an individual entrainment event and (ii) the appearance of homogeneous mixing in an ensemble of entrainment episodes. Furthermore, we demonstrate that the inhomogeneous mixing signature is more pronounced in a polluted cloud, but coarser grid spacing in simulations may compromise the accuracy of this signature. Last, the homogeneous mixing signature results from various equilibrium states established for different entrainment intensities and adjusted wall fluxes, which are challenging to measure experimentally but can be easily analyzed in the simulations.

KEYWORDS: Entrainment; Turbulence; Clouds; Large eddy simulations; Aerosol–cloud interaction; Mixing

1. Introduction

Entrainment of environmental air into a cloud plays an important role in cloud dynamics and microphysics. It affects the lifespan of a cloud (e.g., Jiang et al. 2006; Ghonima et al. 2016), the height of the cloud top (e.g., Lilly 1968; Wood 2012), and the distribution of cloud droplet size (e.g., Latham and Reed 1977; Warner 1973; Mason and Jonas 1974; Wang et al. 2009; Jensen et al. 1985; Yum et al. 2015). These effects impact cloud radiative properties, precipitation formation, and ultimately the entire climate system. Despite its significance, the relationship between turbulence dynamics and entrainment rate remains a major unresolved question in cloud physics (e.g., Driedonks and Duynkerke 1989; Stevens 2002; Wood 2012). Additionally, the way in which the entrainment of subsaturated environmental air affects cloud microphysical properties is under debate (e.g., Lu et al. 2011; Tölle and Krueger 2014; Lehmann et al. 2009; Yeom et al. 2023).

The effect of entrainment of subsaturated environmental air on droplet size distributions (DSDs) can be understood as a combination of two extremes: inhomogeneous and homogeneous mixing. Inhomogeneous mixing occurs when the microphysical response time (τ_{micro}), such as that for single droplet evaporation or for phase relaxation, is significantly shorter than the turbulent mixing time (τ_{mix}), leading to the complete evaporation of all local droplets upon contact with the entrained subsaturated air (Baker et al. 1980). This manifests as a reduction in the droplet number with no change in the shape of the DSD. On the other hand, homogeneous mixing takes place when τ_{mix} is much shorter than τ_{micro}. In this case, all droplets are exposed to the same subsaturated environment, with the consequence that all droplets shrink, altering the

Denotes content that is immediately available upon publication as open access.

Corresponding author: Aaron Wang, aaron.wang@pnnl.gov

DOI: 10.1175/JAS-D-24-0043.1

shape of the distribution but not necessarily the droplet number concentration.

To study the entrainment mechanisms, one can measure DSDs before and after an entrainment event. Ideally, measurements are conducted in the same parcel of air, so that the DSDs before and after mixing can be directly compared. This approach, however, has been difficult to realize. Laboratory experiments by Latham and Reed (1977) show the signature of inhomogeneous mixing by comparing DSDs after an entrainment event to those calculated based on the assumptions of a uniform and homogeneous mixing (e.g., Warner 1973; Mason and Jonas 1974). Studies based on aircraft measurements often diagnose the effect of entrainment on DSDs based on the mixing diagram introduced by Jensen et al. (1985). The type of mixing is inferred by measuring the properties of a cloud affected by entrainment and contrasting them with the assumed initial state, which can be characterized by adiabatic liquid water content computed using the cloud-base height and maximum measured number concentration (e.g., Lehmann et al. 2009). Presumably, this aircraft sampling approach captures entrainment events at various stages of mixing (Haman et al. 2007). The signatures of both homogeneous and inhomogeneous mixing have been observed in aircraft studies: some found more inhomogeneous mixing (Haman et al. 2007; Wang et al. 2009; Lu et al. 2011), some observed more homogeneous mixing (Jensen et al. 1985; Yeom et al. 2017), and some detected signatures of both processes (Lehmann et al. 2009; Desai et al. 2021; Lu et al. 2023). The identification of signatures of homogeneous versus inhomogeneous mixing using aircraft data also depends on the instrument resolution and the degree of averaging, so having higher spatial resolution is advantageous (Haman et al. 2007; Beals et al. 2015). Distance from the cloud top, as well as cloud-top conditions, also influences the degree of inhomogeneity resulting from entrainment (Desai et al. 2021; Yeom et al. 2021, 2024).

Recently, Yeom et al. (2023) performed laboratory experiments to investigate entrainment in the Pi convection-cloud chamber (hereafter "the Pi chamber"; for details, see Chang et al. 2016; Chandrakar et al. 2016). Consistent with previous laboratory experiments by Latham and Reed (1977), they found the signature of inhomogeneous mixing when comparing DSDs immediately upstream and downstream of the entrainment zone. However, when comparing DSDs from different steady-state experiments, the signature was that of homogeneous mixing despite the fact that the mixing appeared inhomogeneous for each steady-state condition. This apparent contradiction in the results from the laboratory may help to explain conflicting results from field campaigns.

To study the entrainment mechanisms with numerical simulations, direct numerical simulations (DNSs) can explicitly resolve the Kolmogorov scale of turbulence. Such simulations have been conducted for limited Reynolds number (Re) because of the demanding computational cost (e.g., Abma et al. 2013; Kumar et al. 2013, 2014, 2018). Kumar et al. (2018) have demonstrated that inhomogeneous mixing becomes more prominent as the domain size increases. To perform DNS for the Pi chamber domain, MacMillan et al. (2022) weakened the gravitational acceleration to reduce the Rayleigh number (Ra) from the order of 10^9 (as in the Pi chamber) to 10^6. The reduced Re increases the Kolmogorov scale, allowing for a coarser grid spacing. Chandrakar et al. (2023) performed DNS and Lagrangian microphysics for a Ra at an order of 10^9, but the horizontal domain is smaller than the Pi chamber. Both MacMillan et al. (2022) and Chandrakar et al. (2023) successfully perform DNS with Lagrangian microphysics to study the microphysical response to supersaturation fluctuations but with corresponding sacrifices in the range of scales represented (either due to limiting the domain size or increasing the dissipation scales).

To simplify numerical simulations, in addition to reducing the Ra and Re for the applicability of DNS (e.g., MacMillan et al. 2022), one can use much coarser grid spacing and apply a subgrid-scale (SGS) model for the unresolved turbulent fluxes, which is large-eddy simulation (LES). Hoffmann et al. (2019) use LES to simulate shallow cumulus clouds with a grid spacing of 20 m. With such grid spacing, they use a linear eddy model to represent the unresolved SGS turbulence effect and the Lagrangian cloud model to resolve the development of DSDs. For the LESs of the Pi chamber with Ra $\sim 10^9$ and a grid spacing of $\sim$3 cm[1] (Thomas et al. 2019; Yang et al. 2022, 2023; Wang et al. 2024a), however, the simulations already resolve the main energy-carrying eddies and take into account the main τ_{mix}. Additionally, a bin microphysics scheme simulates the condensation and evaporation of droplets of various sizes, thereby accounting for τ_{micro}. Although bin microphysics was found to suffer from numerical diffusivity in simulating atmospheric clouds (Morrison et al. 2018; Grabowski et al. 2019), Pi chamber simulations have shown agreement between bin microphysics and the Lagrangian approach which does not suffer from numerical diffusivity (Grabowski 2020; Yang et al. 2023). This is because of the relatively fine grid spacing and the weak particle sedimentation velocity in the simulation of the Pi chamber. Thus, the combination of LES, with appropriate resolution or SGS treatment, and a bin microphysics should be capable of modeling inhomogeneous mixing resulting from entrainment. To verify this hypothesis and further explore the experiment carried out in the Pi chamber (Yeom et al. 2023), we employ LES with a bin microphysics scheme to simulate the experiment and perform sensitivity tests. One critical aspect of this study is that the simulated domain, 4 m^3, is rather small, so the entrainment is resolved at the scale where inhomogeneous mixing can be detected directly.

The rest of the paper is arranged as follows: section 2 introduces the methods, including the setup of the LESs and the implementation of an inlet to introduce the entrainment of subsaturated air. Section 3 presents the results, and section 4 concludes this study. Appendix A explores the entrainment signals at different depths from the top wall. Appendix B shows the remaining DSDs not covered in section 3b. Last, appendix C presents an additional DNS to explain the reason

[1] The $\sim$3-cm grid spacing with a Ra of $\sim 10^9$ is found to fall at the lower end of the inertial subrange (Wang et al. 2024c), justifying the use of an LES framework for this study. A coarser grid spacing falls deeper into the inertial subrange but resolves less details of the flow.

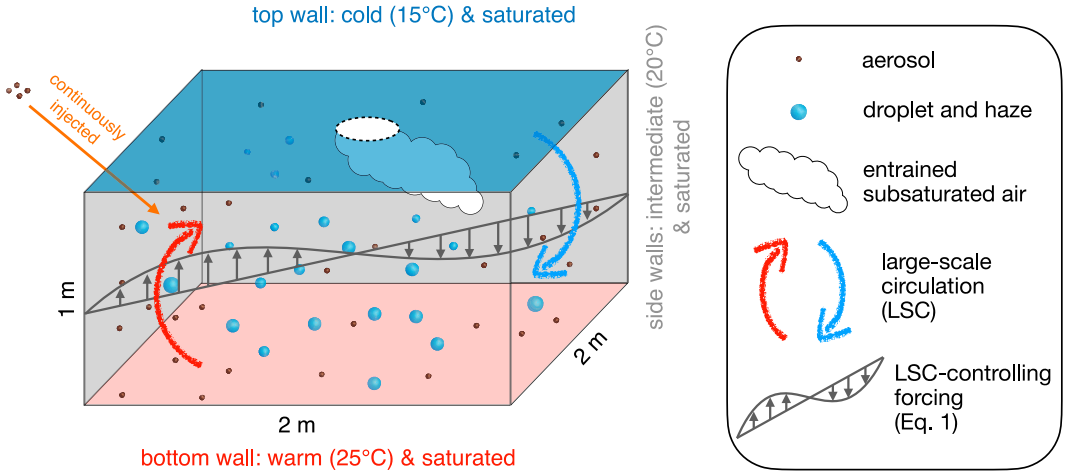

FIG. 1. A schematic of the model setup and simulated objects.

why supersaturation is higher near the bottom than at the top, even without entrainment.

2. Methods

This study will analyze the steady states of clouds with a constant inflow of subsaturated air. The velocity and temperature of the inflowing air are referred to as entrainment velocity and temperature. The simulations are performed to first reach a steady state for the cloud, which is achieved by injecting aerosols into the supersaturated domain driven by a moist, warm bottom and a moist, cold top, as in the Pi chamber. Then, the inlet on the top of the chamber is turned on to introduce the subsaturated air until another steady state is reached. The model setup and simulated objects are summarized in Fig. 1, with details expanded in the following subsections.

a. Large-eddy simulation model

The simulations are conducted using the System for Atmospheric Modeling (SAM), as described by Khairoutdinov and Randall (2003). In this framework, the momentum equations are resolved on an Arakawa C grid, primarily with a uniform 3.125-cm grid spacing in each direction with a domain size of 2 m × 2 m × 1 m. An additional set of runs with a grid spacing of 6.25 cm is later carried out to test the sensitivity to grid spacing (Table 1). The simulations employ an anelastic approximation, a 1.5-order turbulent kinetic energy (TKE) SGS model, and a second-order central advection scheme. The advection of scalars, which includes temperature, microphysical fields, and SGS TKE, is facilitated by a multidimensional positive definite advection transport algorithm (Smolarkiewicz and Grabowski 1990). The eddy diffusivity for scalars within the domain's interior is calculated under the assumption of a turbulent Prandtl number of 1, following the Reynolds analogy (Kays et al. 1980). The boundary conditions for velocities, temperature, and water vapor are determined using the Monin–Obukhov similarity theory (MOST; Monin and Obukhov 1954), with local near-wall velocity, temperature difference, and moisture difference as inputs in a cloud chamber. Because buoyancy is parallel instead of normal to the sidewalls, the MOST applied to the sidewalls is assumed to be in the neutral boundary layer. The roughness lengths for velocity, temperature, and moisture have been tuned to match the DNS results (see details in Wang et al. 2024b). The MOST has not been designed for application under convective conditions without the mean horizontal flow, and wall modeling beneath intense convective flow is known to be challenging (e.g., Wang et al. 2023). However, Wang et al. (2024c) have performed DNS to show that, while the local fluxes near the top and bottom chamber walls modeled by MOST are not the most accurate, the mean fluxes can be matched by tuning the roughness length parameters. We therefore employ this approach in this study. The temperatures are 15°, 20°, and 25°C for the top, side, and bottom walls, respectively. To avoid the complexity from side-wall humidity (Thomas et al. 2019), the water vapor is saturated on all walls with respect to the wall

TABLE 1. Configuration for each simulation. The entrainment RH is 65%. The listed entrainment velocities represent the observed $-w(n_z)$ averaged over the area within the inlet and t = 60–90 min. The seven entrainment cases are carried out under four different conditions to further explore the sensitivity to the aerosol injection rate and grid spacing, resulting in a total of 28 simulations in this study. The seven entrainment cases in the table are performed under four conditions: 1) Aerosol injection rate = 0.15 cm^{-3} s^{-1}; grid spacing = 3.125 cm. 2) Aerosol injection rate = 0.45 cm^{-3} s^{-1}; grid spacing = 3.125 cm. 3) Aerosol injection rate = 0.90 cm^{-3} s^{-1}; grid spacing = 3.125 cm. 4) Aerosol injection rate = 0.45 cm^{-3} s^{-1}; grid spacing = 6.25 cm.

Entrainment case	Entrainment temperature	Entrainment velocity
NOENT	No entrainment	No entrainment
ENT_20°C_Slow	20°C	0.90 ± 0.11 cm s^{-1}
ENT_30°C_Slow	30°C	0.90 ± 0.11 cm s^{-1}
ENT_20°C_Mild	20°C	3.08 ± 0.30 cm s^{-1}
ENT_30°C_Mild	30°C	3.08 ± 0.30 cm s^{-1}
ENT_20°C_Fast	20°C	6.08 ± 0.74 cm s^{-1}
ENT_30°C_Fast	30°C	6.08 ± 0.74 cm s^{-1}

temperatures. The velocity is initially still, and the temperature and water vapor mixing ratio are initially linearly interpolated between the bottom and top values. The buoyancy quickly drives the still air to form a single-roll large-scale circulation (LSC) within the chamber, with the updraft along one sidewall or edge and the downdraft along the other side of the chamber.

The microphysics scheme employed in this study is a haze-enabled bin model, as described in Yang et al. (2023). This model is based on the work of Chen and Lamb (1994) and has been recently implemented into the SAM LES for cloud chamber simulations (Yang et al. 2022, 2023, 2024). Specifically, monodisperse sea salt aerosol particles with a dry diameter of 125 nm are injected in the chamber at a constant rate. Dry aerosols become haze particles of equilibrium size at 90% relative humidity right after the injection. We resolve the activation process by calculating the growth of haze particles by condensation in the same way as cloud droplets. Droplet size distribution is represented by 40 bins with a doubling-mass ratio starting from 0.1 μm. Haze and cloud droplets are particles with radii smaller and larger than 1.0 μm, respectively. The haze and droplets are removed through deposition only on the bottom, not on the top or sidewalls. The heat exchange through the removal of falling droplets is not considered.

The aerosols are homogeneously injected within the domain (Thomas et al. 2019; Wang et al. 2024b), with the injection rate first set at 0.15 $\mathrm{cm^{-3}\ s^{-1}}$, which has been tuned to produce a comparable probability density of number concentration for both haze and droplets, as observed in Yeom et al. (2023). To examine the interaction between the injected aerosols and the entrained subsaturated air, both of which affect the microphysics regime (Chandrakar et al. 2016), we conduct two additional sets of simulations with the aerosol injection rates of 0.45 and 0.90 $\mathrm{cm^{-3}\ s^{-1}}$ (Table 1).

To compare cloud microphysical properties immediately before and after the mixing of subsaturated air with the cloudy air parcel following the LSC, we place virtual sensors at the upstream and downstream areas with respect to the entrainment inlet. These locations of the virtual sensors are similar to those of the real sensors in the Pi chamber (Yeom et al. 2023). When recording the temporal fluctuations (as shown in Figs. A1 and A2), the results are obtained from every time step recorded in a specific grid cell. When showing the mean microphysical properties (as presented later in Figs. 5, 6, 10, and B1–B3), to enhance the robustness of the statistics, we average the results over the horizontally 3×3 grid cells and the time period of t = 60–90 min. Regarding the wind direction near the entrainment inlet, Yeom et al. (2023) took advantage of the fact that the LSC is mostly locked in place in the chamber owing to the imperfect temperature distributions in the panels, access ports, viewing windows, and the tilt of the top and bottom surfaces (Anderson et al. 2021). In contrast, in the idealized simulations without these interferences, the LSC of the Rayleigh–Bénard convection naturally changes its orientation over time (see the detailed review of the LSC orientation variation in Ahlers et al. 2009, section VIII.A). To control the orientation of the LSC and have the ability to compare cloud microphysical properties immediately before and after entrainment, we impose the following forcing term in the prognostic equation for the vertical velocity component as follows:

$$\left(\frac{\partial w}{\partial t}\right)_{\mathrm{LSC}} = F \sin\left(\frac{z\pi}{l_z}\right)\left[\cos\left(\frac{x\pi}{l_x}\right) + \cos\left(\frac{y\pi}{l_y}\right)\right], \tag{1}$$

where l_x, l_y, and l_z are the x, y, and z lengths of the domain and $F = 0.6\ \mathrm{cm\ s^{-1}}$ is the scale of LSC forcing. Though it is observed that the LSC still changes its direction occasionally, it quickly reverts back to its preferred orientation, reaching a steady state for analysis. This forcing mechanism ensures that the LSC maintains a consistent direction for the majority of the simulation time. Although this approach comes with a trade-off of an increase in the total TKE by approximately 17% compared to the simulation without imposing the forcing, other approaches, e.g., imposing a temperature difference on opposite sides of the chamber (Huang and Zhang 2023; Wang et al. 2024b), cause further changes to the scalar fields in addition to the momentum field.

The configurations for all simulations are summarized in Table 1. Specifically, we perform seven entrainment cases (hereafter referred to as "cases") to test the influences of various temperatures and velocities of the entrained air, under four different conditions (hereafter referred to as "conditions"), involving various aerosol injection rates and grid spacings, resulting in a total of 28 simulations. Each case is named based on whether entrainment is initiated, the temperature of the entrained air, and the entrainment velocity. The entrainment velocity is induced by an imposed forcing, which is detailed in the next subsection, at the highest grid level for nonzero vertical velocity and within the area of the inlet. The "NOENT" case does not involve any entrainment. The remaining cases are listed in ascending order of entrained air temperature and vertical velocity. The relative humidity (RH) of the entrained air is set to 65%. For cases with an injection rate of 0.45 $\mathrm{cm^{-3}\ s^{-1}}$, an additional grid spacing of 6.25 cm is tested. All 28 simulations are performed for a physical time of 90 min. Except for the NOENT case, the inlet is opened at t = 30 min, and the results are averaged over the period from t = 60 to 90 min.

b. *A pseudo inlet for subsaturated air*

To introduce the subsaturated air into the cloud chamber requires an open boundary condition for part of the top wall. However, the local modification to the boundary condition is not applicable to the model pressure solver that derives the pressure field from a Poisson equation solved in the Fourier space in SAM. The impracticability of creating a local inlet in the Fourier space leads us to introduce a "pseudo inlet," which modifies the boundary conditions with the addition of advection-based forcings for velocities, temperature, and water vapor mixing ratio. We then let the pressure field adjust accordingly, which may induce an adverse pressure gradient force against the added velocity forcing, leading to a reduced effective entrainment velocity and, subsequently, to an underestimated depth of the entrainment layer. In the real Pi chamber, as subsaturated air is pumped in, the pressure within the

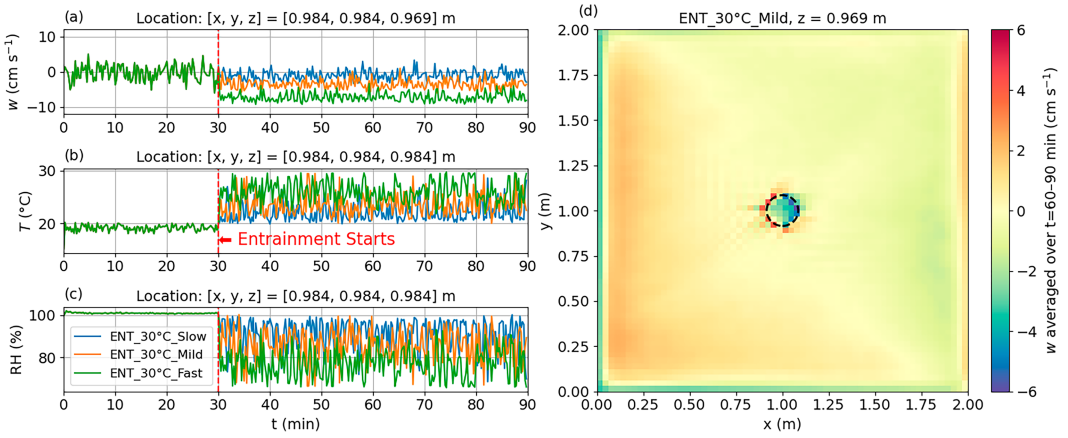

FIG. 2. The time series (sampled every 30 s) measured near the center of the highest grid level of (a) w, (b) T, and (c) RH from the three chosen cases: ENT_30°C_Slow (blue line), ENT_30°C_Mild (orange line), and ENT_30°C_Fast (green line), with an aerosol injection rate of 0.15 cm^{-3} s^{-1}. (d) The w at the nz-1 level averaged over t = 60–90 min from the ENT_30°C_Mild case, with the black dashed line indicating the edge of the pseudo inlet area.

chamber rises slightly, causing mass to leak out through unsealed regions, and thus, the local pressure resistance should not be as strong. Nevertheless, we will later demonstrate that the artificial inflow of subsaturated air in the model is sufficient to investigate the cloud's microphysical response to entrainment observed in the Pi chamber.

The pseudo inlet located at the top center has an inlet radius of 8.5 cm, identical to that in the Pi chamber experiments. The boundary conditions for velocity and scalars within this area are governed by the SGS model instead of the wall model. For the SGS model for the grid points adjacent to the pseudo inlet, it is assumed that at or beyond the top boundary, the horizontal velocities are zero; the vertical velocity matches that at the grid level adjacent to the top boundary; and the temperature and moisture conditions follow those described in Table 1. To replicate the inflow used in the experiment by Yeom et al. (2023), we apply a forcing to the vertical velocity at the grid level adjacent to the top boundary and within the inlet area as follows:

$$F_{w,\text{inlet}} = \frac{w_{\text{ent}} - w(n_z)}{\Delta t_{f,w}}, \tag{2}$$

where w is the vertical velocity, n_z indicates the grid level adjacent to the top boundary, $\Delta t_{f,w} = \Delta z / w_{\text{ent}}$, and w_{ent} denotes the intended entrainment velocity. This forcing aims to restore $w(n_z)$ to the value of w_{ent}, but the actual measured $w(n_z)$ is weaker than w_{ent} because of the adverse pressure gradient force. Consequently, the entrainment velocities listed in Table 1 represent the actual $w(n_z)$ values. For moisture and temperature, we introduce the virtual advection terms to the grid cells by the top boundary within the inlet area as follows:

$$\text{ADV}_{\phi,\text{virtual}} = -w(n_z)\frac{\phi_{\text{ent}} - \phi(n_z)}{\Delta z}, \tag{3}$$

where ϕ represents either the temperature or water vapor mixing ratio. The variable ϕ_{ent} denotes either the temperature listed in Table 1 or the corresponding water vapor mixing ratio with an RH of 65%.

To illustrate the effects of the pseudo inlet, we use the results with the entrainment air of 30°C, as depicted in Fig. 2. The time series of w near the top center confirms the onset of an inflow subsequent to the commencement of entrainment (Fig. 2a). The temporal-averaged w near the top boundary shows, in addition to the LSC, an updraft at the upwind edge of the pseudo inlet area compensating for the downdraft within the inlet (Fig. 2d). The temperature and RH data show that turbulent fluctuations occasionally reach the entrained value, and their mean values are closer to the entrained values as the entrainment velocity increases (Figs. 2b,c).

3. Results

Figure 3 provides a visualization of the flow field, using the ENT_20°C_Fast case as an example. It displays snapshots of three-dimensional isosurfaces and vertical slices of temperature and supersaturation. The LSC can be observed carrying warm air upward from the near-left corner and cold air downward from the far-right corner, in agreement with a single-cell LSC observed in the Pi chamber. Subsaturated air is entrained at the central top region, with the downwind direction pointing toward the far-right corner. As the scalar field within the domain is not uniformly mixed, the sensor, while attempting to capture the local influence of the entrainment near the top wall, is simultaneously influenced by the colder and drier top boundary (as indicated by the blue color near the top in Fig. 3b). In the following subsections, we will quantitatively analyze the temporal evolution of domain-averaged properties, DSDs, and homogeneous/inhomogeneous signatures.

a. Evolution of domain-averaged properties

Here, we use RH and droplet liquid water content (LWC) to illustrate the mean thermal and microphysical conditions simulated in the chamber. The simulations start with a supersaturated environment (with temperature and moisture

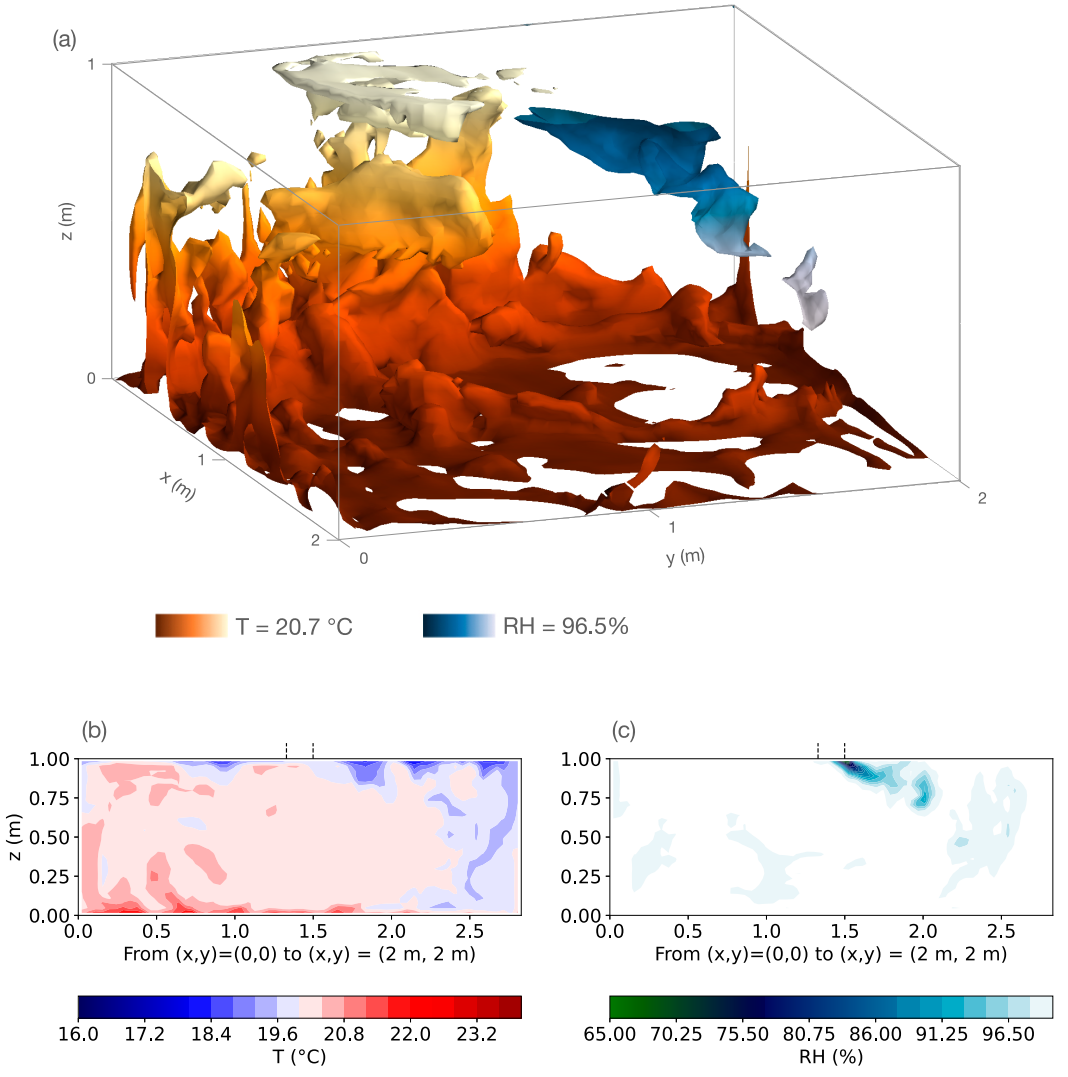

FIG. 3. Visualization of the flow fields featuring (a) three-dimensional isosurfaces of temperature and RH, (b) the temperature field on a diagonal slice extending from $(x, y) = (0, 0)$ to $(x, y) = (2, 2$ m), and (c) the RH field on the same slice. The dashed lines above the top of the frames in (b) and (c) indicate the location of the pseudo inlet. The snapshot is taken at $t = 74$ min from the ENT_20°C_Fast case with an aerosol injection rate of 0.15 cm^{-3} s^{-1}.

linearly interpolated between the warm, saturated bottom and the cold, saturated top) and the constant injection of aerosols. Condensation on aerosols forms cloud droplets, which consumes RH and increases LWC, and the cloud droplets are eventually removed by deposition so that a steady state is reached. As shown in Figs. 4a and 4b, for an aerosol injection rate of 0.15 cm^{-3} s^{-1}, both RH and LWC reach a steady state within 20 min. After entrainment starts, the steady states of RH and LWC are reestablished within another 10 min. This justifies using the results averaged over $t = 60$–90 min for subsequent analysis.

Figures 4c–h show that as the aerosol injection rate rises, the time for both RH and LWC to reach steady states increases. At $t = 30$ min, before entrainment begins, the RH is still slightly decreasing and LWC is slightly increasing for a higher aerosol injection rate. This is due to the reduced droplet size and settling velocity (reflected by the increased LWC). However, after entrainment begins, compared to the condition in which the aerosol injection rate is 0.15 cm^{-3} s^{-1}, the RH achieves a steady state in a shorter period of time for aerosol injection rates of 0.45 and 0.90 cm^{-3} s^{-1}. This shorter time may reflect the phase relaxation time, which is proportional to NC$^{-2/3}$, where NC is the droplet number concentration that increases with the aerosol injection rate (Chandrakar et al. 2016). In some cases, the LWC continues to increase slightly after the RH reaches a steady state because of the reduced depositional removal with the smaller droplet size, but the slightly increasing NC does not affect the study's conclusions.

b. *Analysis of droplet size distributions*

We place three virtual sensors in the upwind, central, and downwind regions. The sensors are 7.8 cm from the top wall, with the upwind and downwind sensors each located 15 cm

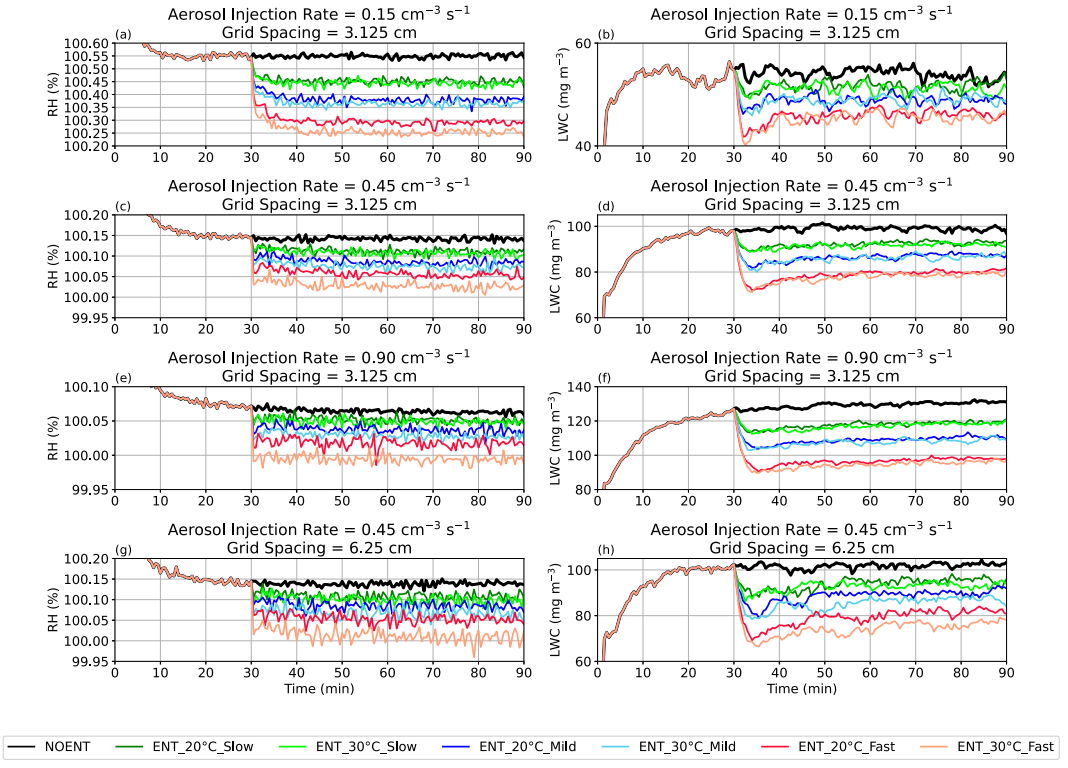

FIG. 4. Time series of domain-averaged (a),(c),(e),(g) RH and (b),(d),(f),(h) droplet LWC. The droplet LWC does not include the haze component.

from the horizontal center. The vertical location is where all cases can detect the entrainment signals as explored in appendix A. To examine the DSDs in different regions for each case, we use the simulations with an aerosol injection rate of 0.15 cm^{-3} s^{-1} as an example, as shown in Fig. 5. For comparison, the downwind DSD of the NOENT case is plotted as a black dashed line. The DSDs under the remaining three conditions can be found in appendix B. In Fig. 5, each case reveals distinct peaks for haze and droplets with comparable values, in line with the observations reported in Yeom et al. (2023). Given that the responses of haze and droplets to entrainment vary in certain instances, we use a cutoff diameter of 2 μm, roughly the critical size of the injected sea salt aerosol, to differentiate between haze and droplets hereafter. If not specified, the properties to which we refer are for droplets only. However, when we refer to DSD, we include the size distribution of both.

In each case, moving from the upwind to the downwind regions, the peak NC decreases—a trend that is more pronounced with stronger entrainment velocities and higher entrainment temperatures. Although the NC decreases, the peak diameter remains similar, which is a characteristic indicative of inhomogeneous mixing as reported in Yeom et al. (2023). However, the NC of haze does not consistently decrease in the downwind region. The NC of haze shows a similar trend only when the aerosol injection rate is as high as 0.90 cm^{-3} s^{-1} (see appendix B).

Our focus to this point has been on a comparison of the DSD immediately before the entrainment zone to the DSD immediately afterward. This comparison shows little changes in the DSD shape, which is indicative of inhomogeneous mixing. However, Fig. 5 also allows a comparison of the DSDs among the different steady-state experiments. A careful examination of the differences in DSDs between the NOENT case and the entrainment case in each of the six panels shows that an increase in the entrainment velocity and/or an increase in the temperature of the entrained air leads to a decrease in the mean droplet size and an increase in NC. The comparison between the DSDs with entrainment and NOENT (or between DSD with different entrainment conditions) seems to indicate homogeneous mixing. These changes in the mean droplet diameter and NC will be analyzed further below.

While comparison of the DSDs among the different entrainment conditions points to homogeneous mixing, it is important to note that these are not DSDs representing the response of the cloud before and after a mixing event. DSDs from the different experiments represent the steady-state response of the cloud to a particular set of fluxes, which include vapor from the chamber surfaces and subsaturated air from the entrainment inlet. If, for example, the entrainment velocity increases, the steady-state microphysical properties of the cloud adjust to the new, drier conditions with a decrease in the mean droplet size. (Somewhat counterintuitively, this can lead to an increase in the droplet concentration because the residence time of the smaller droplets is longer owing to the reduced fall velocity.)

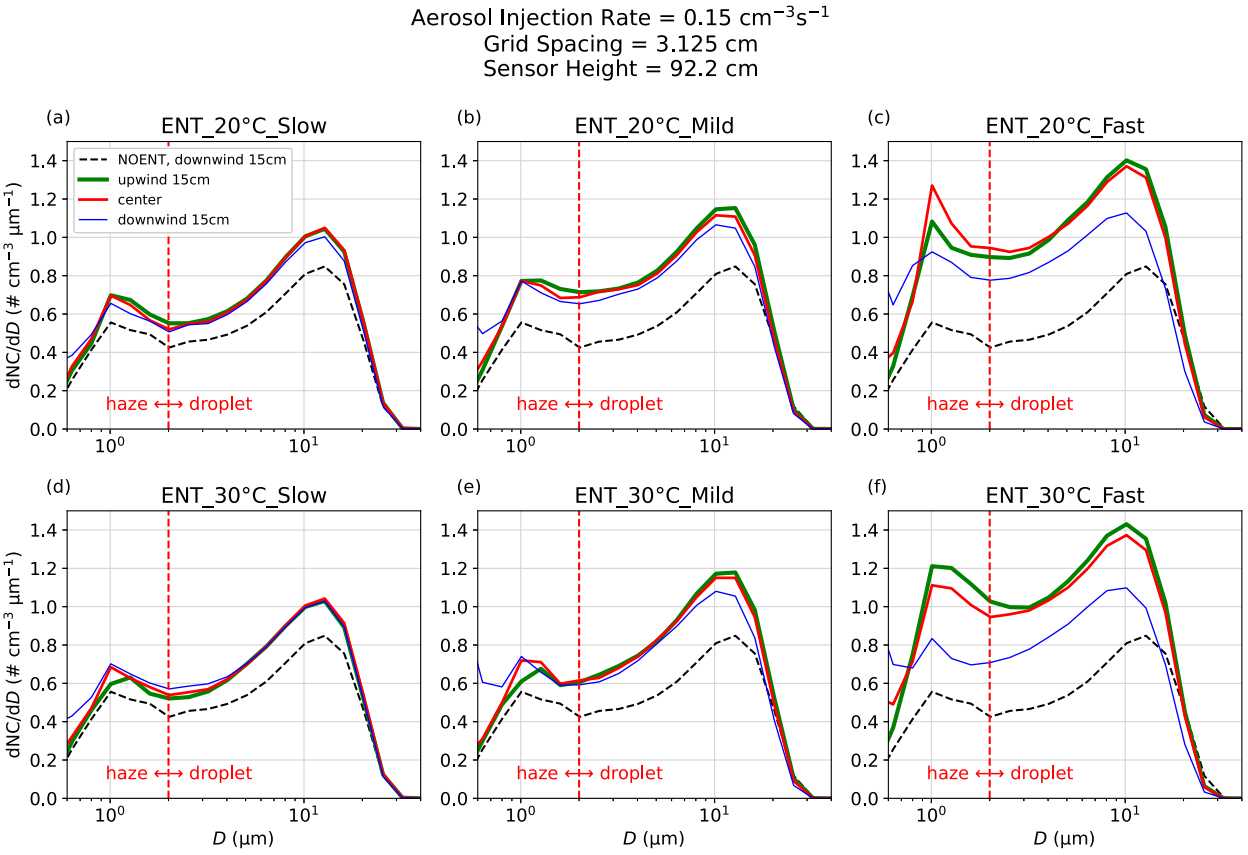

FIG. 5. Upwind, central, and downwind DSDs, measured at $z = 92.2$ cm, for the simulations with an aerosol injection rate of 0.15 cm^{-3} s^{-1}. The downwind DSD for the NOENT case (shown as a black dashed line) is included for comparison. The red dashed line indicates the cutoff diameter used to distinguish between droplets and haze.

c. *Evaluation of mean liquid water content, droplet diameter, and number concentration*

The mean properties calculated in this section only consider droplets with sizes larger than 2 μm (see the red dashed line in Fig. 5), and the discussion first focuses on the results with an aerosol injection rate of 0.15 cm^{-3} s^{-1}. Figure 6a reveals that in the ENT_20°C_Slow and ENT_30°C_Slow cases (represented in dark and light green), the changes in NC from upwind to downwind regions are relatively small. This suggests that the reduction in LWC is mostly due to a decrease in the droplet size, a signature of homogeneous mixing. As the entrainment velocity increases, the reduction in NC also intensifies, but the variation in the droplet size remains similar, implying an enhanced characteristic of inhomogeneous mixing. This trend can be quantified by the slopes of the virtual lines connecting the upwind and downwind data points (Table 2).

As noted above, when comparing different steady-state experiments, the reduction in droplet size becomes significant as the entrainment velocity and temperature increase. The droplet concentration even increases because the smaller droplets settle more slowly, reducing deposition removal. As the state of the system adjusts to the balance of fluxes, the cloud microphysical properties may have the signature of homogeneous mixing. When the domain average is considered, the relationships between the droplet size and liquid water content display a roughly linear pattern (represented by the cross-markers in Fig. 6). This pattern indicates a balance among evaporation, turbulent mixing, and deposition removal.

Figure 7 displays the spatial distribution of the temporally averaged D and LWC for an aerosol injection rate of 0.15 cm^{-3} s^{-1}. In most areas across all cases, the variation in D largely follows the pattern of LWC. This suggests that the majority of the domain (i.e., the volume of the chamber) undergoes homogeneous mixing. Evidence of inhomogeneous mixing is apparent only near the entrainment region when the entrainment velocity is sufficiently strong.

d. *Enhancement of inhomogeneous mixing by pollution*

Inhomogeneous mixing becomes more significant as τ_{micro} decreases. Given that the evaporation time is proportional to the square of the droplet diameter (Yau and Rogers 1996), simulations with higher pollution levels (i.e., increased aerosol injection rates), which result in smaller mean droplet sizes (Chandrakar et al. 2016), are expected to show a stronger signature of inhomogeneous mixing. This is confirmed in Figs. 6b and 6c (cf. Fig. 6a) and Table 2, where an increased

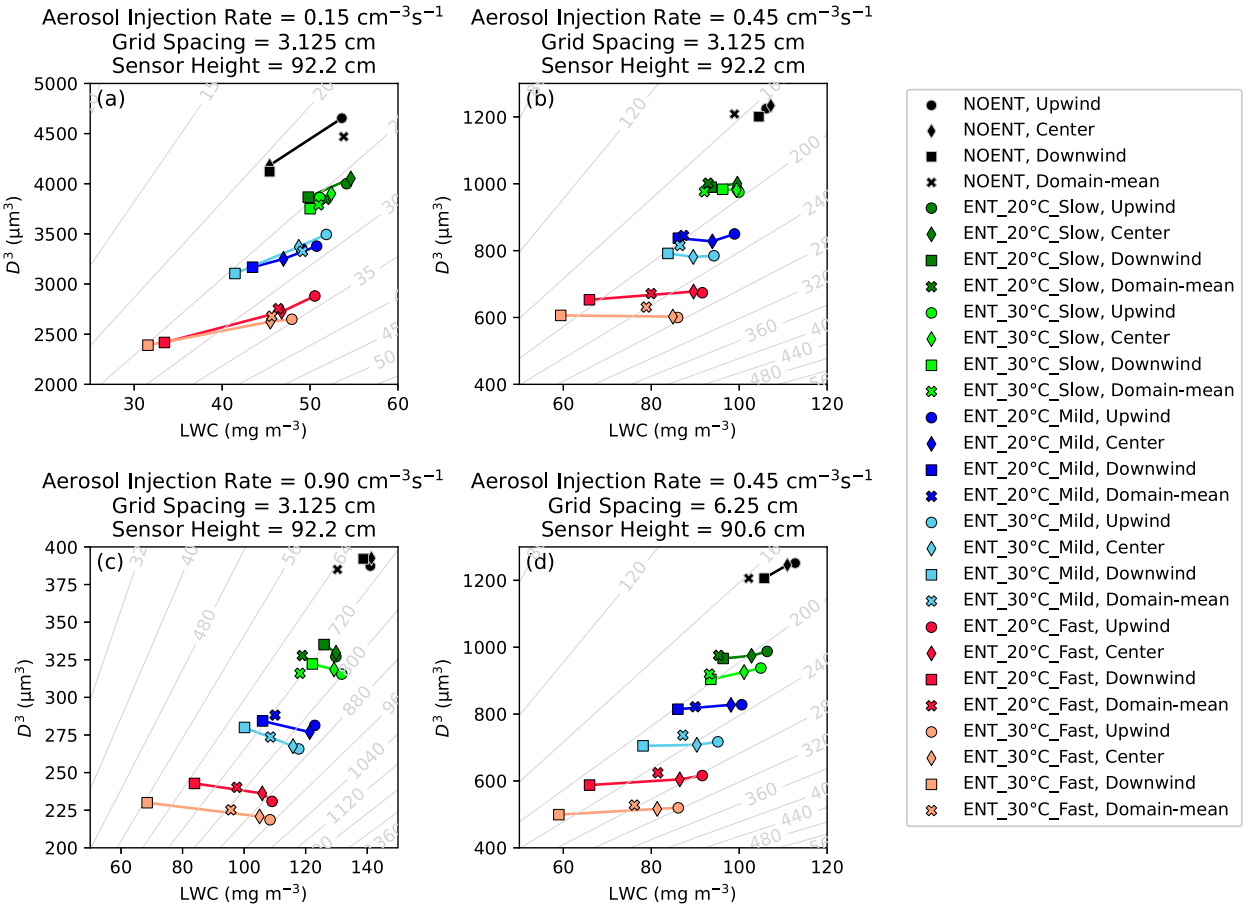

FIG. 6. Mean droplet diameter cube vs LWC in each case (differentiated with colors) at upwind, central, and downwind regions (differentiated with markers). The gray contour line represents the droplet number concentration (cm^{-3}), calculated as NC = 6LWC/($\rho_w \pi D^3$), where ρ_w = 1 g cm^{-3} is the density of liquid water. Note that the real mean number concentration depends on DSD and may differ from the value calculated assuming a single size. The results are averaged over t = 60–90 min.

aerosol injection rate results in a more pronounced reduction in the liquid water content at the downwind region, while the droplet size remains relatively constant in each entrainment case. In some cases, the downwind mean droplet size even increases, possibly because larger droplets evaporate later while small droplets have already evaporated.

TABLE 2. The upper part of the table shows the condition and corresponding panels in Fig. 6 and the lower part of the table shows the slopes of the virtual lines connecting upwind and downwind data points in Fig. 6 (μm^3 m^3 mg^{-1}). A shallower slope implies a more pronounced inhomogeneous mixing. (a)–(d) The panels in Fig. 6.

Figure 6	(a)	(b)	(c)	(d)
Aerosol injection rate (cm^{-3} s^{-1})	0.15	0.45	0.90	0.45
Grid spacing (cm)	3.125	3.125	3.125	6.25
ENT_20°C_Slow	30.7	−1.15	−2.08	2.11
ENT_30°C_Slow	103.5	−2.25	−0.70	2.96
ENT_20°C_Mild	28.8	0.99	−0.17	0.93
ENT_30°C_Mild	37.5	−0.67	−0.81	0.72
ENT_20°C_Fast	27.1	0.81	−0.47	1.11
ENT_30°C_Fast	15.8	−0.23	−0.28	0.75

Figure 8 shows the spatial distribution of D and LWC for each case with an aerosol injection rate of 0.45 cm^{-3} s^{-1}. Except near the entrainment inlet, the LWC is higher in the upwind region and lower in the downwind regions of the LSC. Although D also exhibits higher values in the upwind region and lower values in the downwind regions of the LSC, an additional peak appears in the center of the domain. This peak in D represents an increased signature of inhomogeneous mixing across the domain because the variation of D starts to deviate from the typical variation pattern of LWC.

The signature of inhomogeneous mixing dominates across the domain when the aerosol injection rate is increased to 0.90 cm^{-3} s^{-1}. Figure 9 reveals that while the LWC still follows the pattern of the LSC, the variation in D is dependent solely on the distance from the walls, not on the LSC. This spatial deviation between the D and LWC patterns is also evident even in the absence of entrainment, as demonstrated by the wall effects in Fig. 9a.

To further explain the spatial distribution of D without entrainment, we compare the supersaturation (defined as RH-100%) and the DSDs in the NOENT cases with three aerosol injection rates. Figure 10 shows how the supersaturation

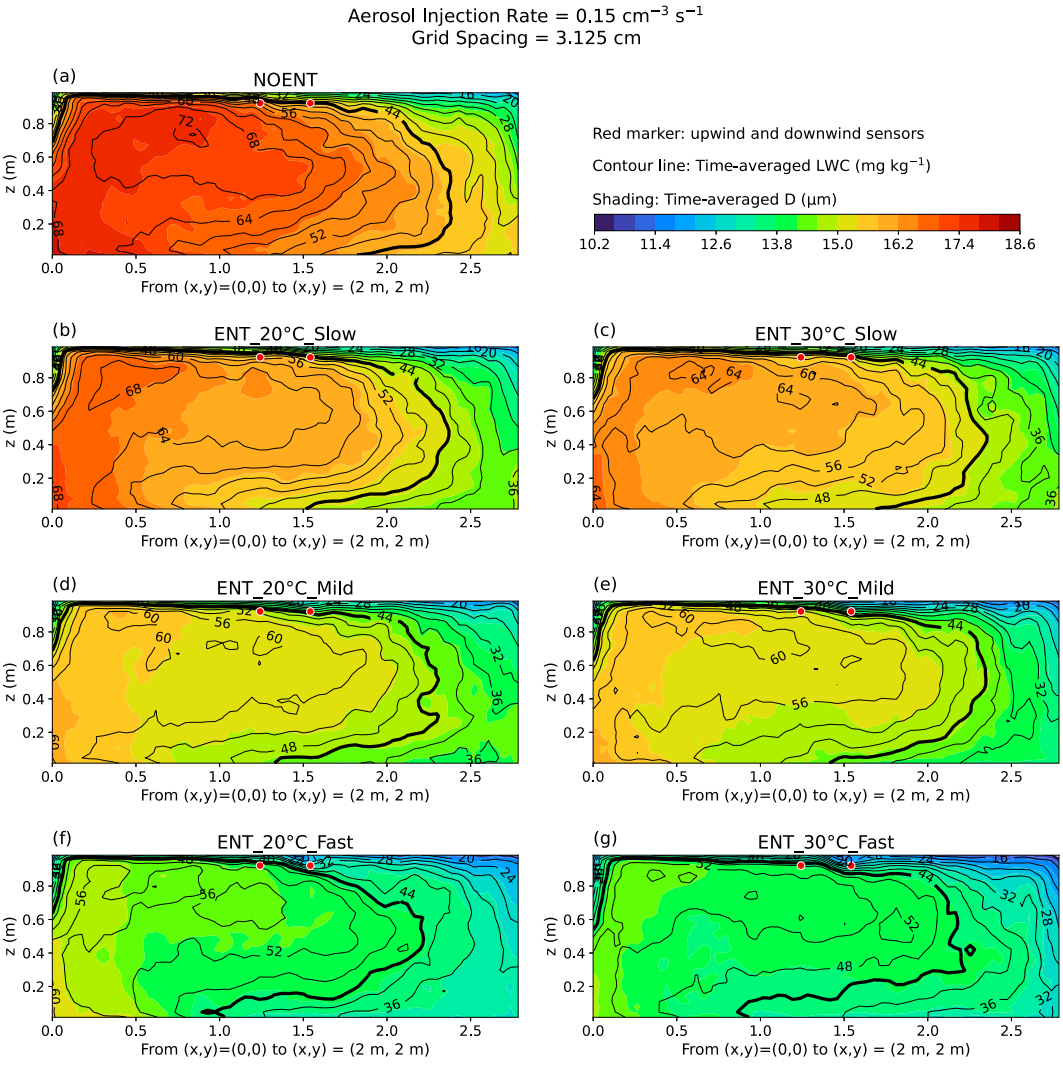

FIG. 7. Diagonal slice of the droplet diameter (represented by shading) and LWC (indicated by contour lines; the thick line corresponds to a value of 44 mg kg^{-1}), averaged over t = 60–90 min in each clean simulation. The red markers denote the upwind and downwind locations of sensors that record the data presented in Figs. 5 and 6.

following the LSC is affected by the wall fluxes: The supersaturation is the highest near the bottom of the updraft (see the reason explored in appendix C), decreases when the air parcel ascends by the sidewalls, slightly increases again by the top wall to the downdraft region, and then decreases again when the air parcel descends. The NC peak is the highest at the base of the updraft (sensor 1 in Figs. 10d–f) and decreases in the less-saturated near-wall regions as the parcel moves with the LSC. The NC peak reaches its lowest values at sensor 5 for the aerosol injection rates of 0.15 and 0.45 cm^{-3} s^{-1} and roughly at sensors 6 and 7 for the aerosol injection rates of 0.90 cm^{-3} s^{-1}. When the aerosol injection rate is 0.15 cm^{-3} s^{-1} (Figs. 10a,d), the wall fluxes affect DSD in a way similar to the homogeneous mixing with the entrained subsaturated air. When the aerosol injection rate is 0.45 cm^{-3} s^{-1} (Figs. 10b,e), the change of the droplet size is reduced, showing more similarity to the inhomogeneous mixing signature. When the aerosol injection rate is 0.90 cm^{-3} s^{-1} (Figs. 10c,f), the NC variation exhibits almost no change in the droplet size, a signature of inhomogeneous mixing. However, such a signature is caused by the less-saturated near-wall regions instead of the entrainment of subsaturated air.

The sensor at the center (sensor 9 in Fig. 10) has relatively low supersaturation. The likely reason is that this part of the domain is farthest from the boundaries and is most well mixed. Mixing in the presence of gradients forces the supersaturation in this flow, so being well mixed and far from boundaries suggests weak forcing. When the aerosol injection rate is 0.15 cm^{-3} s^{-1} (Figs. 10a,d), sensor 9 detects the highest NC across all sizes, possibly because the small droplets do not grow (owing to the low supersaturation), while it catches the larger droplets falling from the updraft (revealed by Fig. 6a). When the aerosol injection rate is 0.90 cm^{-3} s^{-1} (Figs. 10c,f), the small droplets ($D \sim 4$ μm) near the center are fewer in

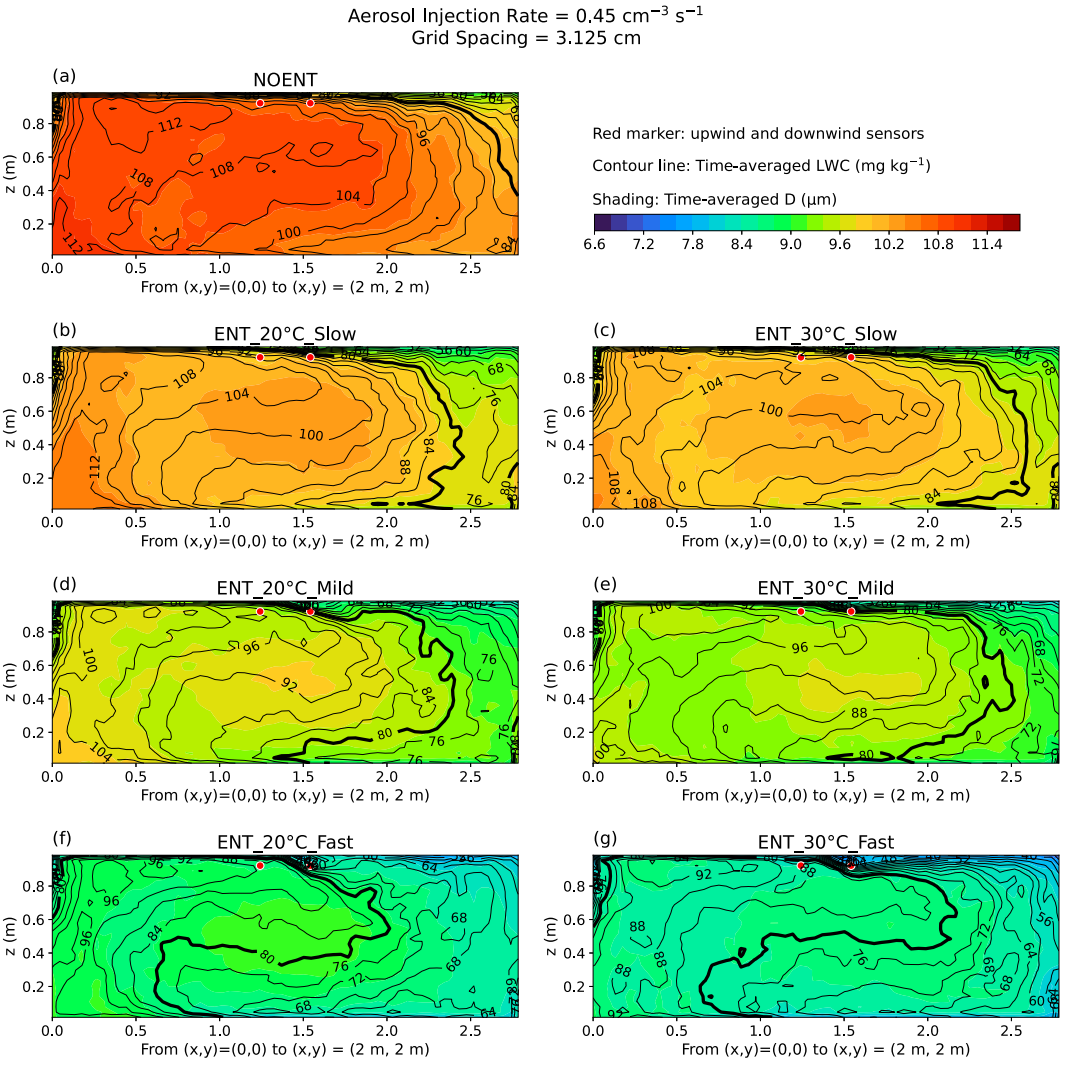

FIG. 8. As in Fig. 7, but for the cases with an aerosol injection rate of 0.45 cm^{-3} s^{-1}, and the thick contour line now represents a value of 80 mg kg^{-1}.

number than other locations because of the deactivation by low supersaturation, but the central region may still capture the large droplet falling from the updraft, resulting in a higher mean droplet diameter there (Fig. 9a).

e. *Reduced inhomogeneous mixing signature with rougher grid spacing*

Inhomogeneous mixing can be captured by LES with fine grid spacing owing to its ability to resolve energy-carrying eddies and the mixing carried by them. However, LES grid spacing is supposed to fall in the inertial subrange instead of to resolve the inhomogeneous mixing process. As most LES SGS mixing is assumed to be homogeneous, an increase in grid spacing may reduce the observable signature of inhomogeneous mixing. This hypothesis is supported by a comparison between Figs. 6b and 6d (as quantified in Table 2, columns b and d), where the reduction in droplet size in the downwind region becomes more apparent as the grid spacing increases from 3.125 to 6.25 cm for most cases (the only exception is the ENT_20°C_Mild case). Note that the DNSs with similar Re and Ra performed by Wang et al. (2024c) demonstrate that both 3.125 and 6.25 cm fall within the inertial subrange.

The spatial distribution of D and LWC shows that the big picture of the patterns is similar with both grid spacings of 3.125 and 6.25 cm (cf. Fig. 11 to Fig. 8). The peak of D at the center of the domain, which signifies the increase of inhomogeneous mixing, is still present with a grid spacing of 6.25 cm. Thus, at least in this study, the sensitivity of inhomogeneous mixing signature to grid spacing is relatively local and detailed; the big pattern is not sensitive to grid spacing.

f. *The response of systems as revealed by wall fluxes*

As discussed above, the signature of homogeneous mixing is a result of the system relaxing to a different steady-state

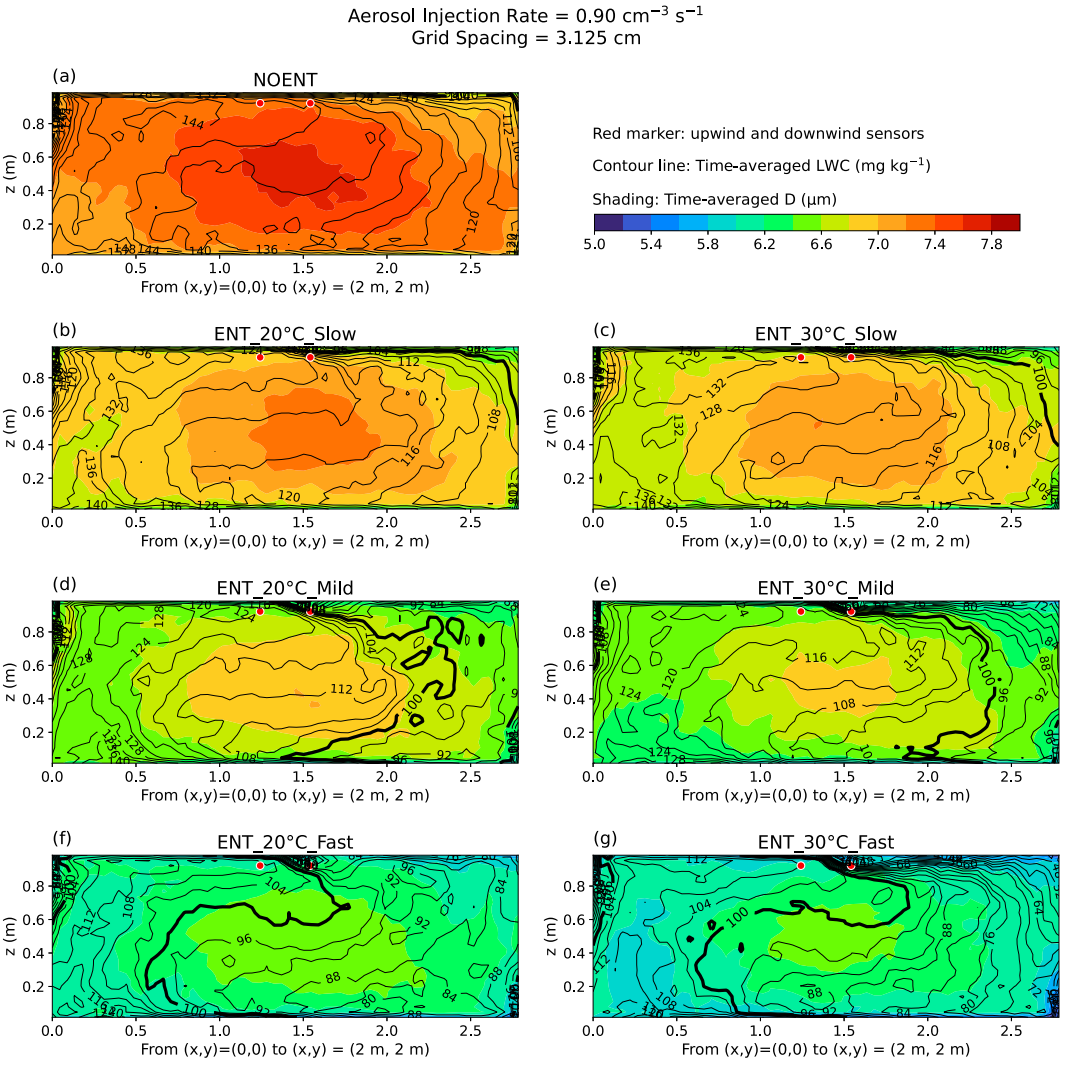

FIG. 9. As in Fig. 7, but for the cases with an aerosol injection rate of 0.90 cm^{-3} s^{-1}, and the thick contour line now represents a value of 100 mg kg^{-1}.

condition for given, constant boundary fluxes (Yeom et al. 2023). While measuring boundary fluxes is challenging in the real Pi chamber, LES can easily output these fluxes for analysis. Figure 12 illustrates the wall (including the side, top, and bottom walls) heating and evaporation rates, which are the sensible heat flux and moisture flux, respectively, multiplied by the wall areas excluding the inlet area.

The heating rate shows that the walls function as heat sinks to balance the latent heat released by condensation, the latent heat absorbed by evaporation owing to the entrainment, and the extra heat carried by the entrained air (Figs. 12a,c,e,g). Specifically, as the entrained air temperature remains at the mean of the walls (20°C), the cooling effect of the wall decreases because of the additional evaporation cooling (see the green, blue, and red lines in Figs. 12a,c,e,g). When the entrained air is warmer (30°C), the walls' cooling effect intensifies to offset the extra heat (see the light green, light blue, and pink lines in Figs. 12a,c,e,g).

The evaporation rate indicates that when the entrained air is 20°C, the walls function as moisture sources (Figs. 12b,d,f,h) to balance the water vapor that is condensed and removed by deposition. Increasing the entrainment velocity enhances the total wall evaporation rate. However, when the entrained air rises to 30°C and keeps an RH of 65%, the entrained water vapor mixing ratio (~17.9 g kg^{-3}) exceeds the saturation values at the top wall (~10.8 g kg^{-3}) and sidewalls (~14.9 g kg^{-3}), causing the total condensation rate on the top and sidewalls to exceed the evaporation rate on the bottom wall. Therefore, an increased entrainment velocity enhances the total wall condensation rate.

Taking these two results together, we see that the microphysical properties of the cloud are a result of the totality of the fluxes in the system. If any of the fluxes change (e.g., an increase in the flux of subsaturated air through entrainment), the system response [with a time scale on the order of tens of seconds to minute (Yeom et al. 2023)] results in new

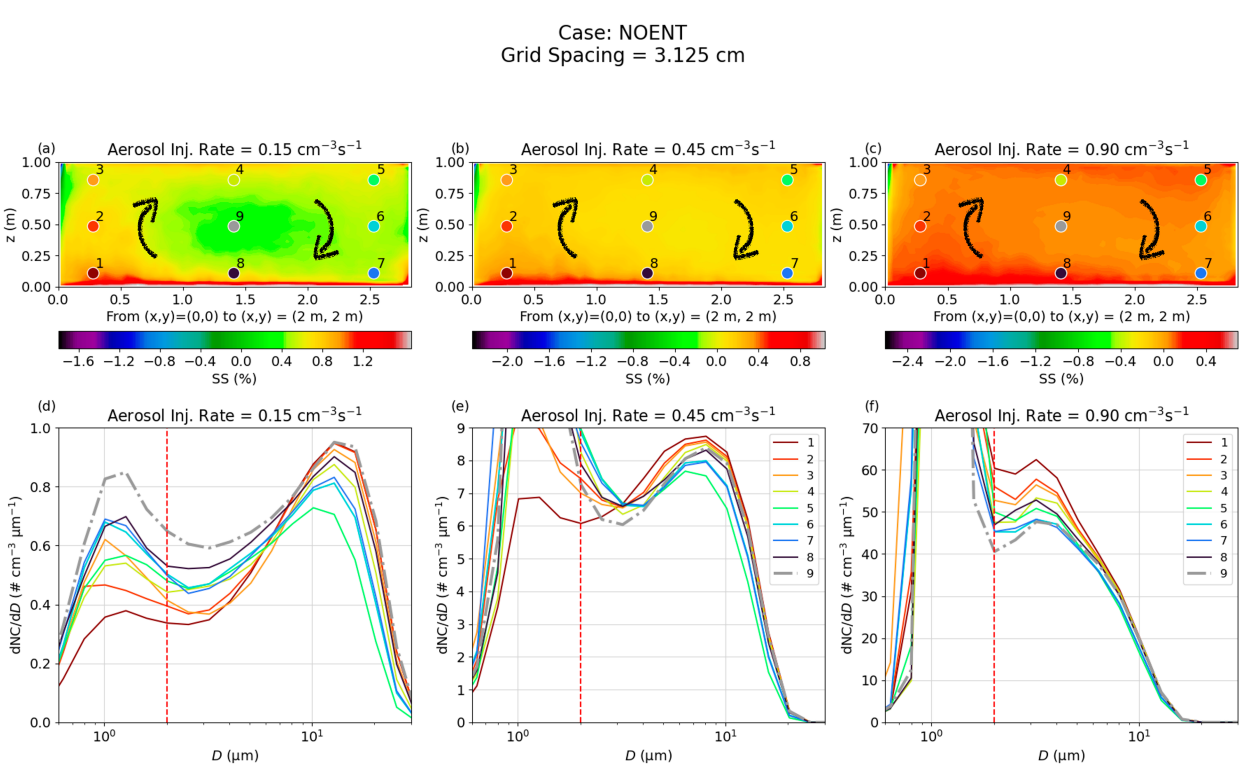

FIG. 10. (a)–(c) The supersaturation (with black arrows indicating the direction of LSC) and (d)–(f) the DSDs in the NOENT cases with various aerosol injection rates averaged over t = 60–90 min. The locations of the DSDs in (d)–(f) correspond to those in (a)–(c). As in Fig. 5, the red dashed lines in (d)–(f) separate haze and droplets. (e),(f) Since the focus is on the cloud droplets, we allow the haze–droplet part of the distribution to exceed the y axis limits, thereby enabling better visualization of variations in the cloud-droplet distribution.

microphysical properties. If drop size distributions from before the flux adjustment and afterward are compared, the signature can be reminiscent of homogeneous mixing (see Fig. 4 in Yeom et al. 2023). However, we make the distinction here that inhomogeneous and homogeneous mixing are properly understood as comparisons of air masses immediately before and after mixing.

4. Conclusions and discussion

The impact of entrainment on cloud microphysical properties can manifest as either homogeneous or inhomogeneous mixing signature. Previous laboratory experiments with the Pi chamber by Yeom et al. (2023) showed signatures of locally inhomogeneous mixing for individual entrainment experiments and homogeneous mixing when analyzing an ensemble of experiments with different entrainment velocities and temperatures. The mechanisms behind the response of cloud droplets to mixing depend on the turbulent mixing and droplet evaporation time scales, which can be resolved using LESs and bin microphysics, respectively. Thus, we employ LESs and bin microphysics to show the feasibility of such methods, confirm the observations from the Pi chamber, and explore the phenomena in greater depth.

Reproducing the Pi chamber experiments using LES presents two main technical challenges. The first challenge is to guide the LSC to accurately capture the upwind and downwind regions of the entrainment zone. This is addressed by imposing a wavy forcing on the vertical velocity. The second challenge is to create an input for entrainment. We handle this by employing a pseudo inlet method that introduces a forcing for vertical velocity with additional advection terms for the scalars. Our results affirm that subsaturated air is introduced into the domain with a reasonably shaped plume.

Upon successfully incorporating the LSC and entrainment mechanisms into the model, our study provides several important insights. When the aerosol injection rate is set at 0.15 cm^{-3} s^{-1} and the entrainment velocity is slow, entrainment displays characteristics of locally homogeneous mixing. As the entrainment velocity increases, the signature of local inhomogeneity is enhanced, but the overall mixing across the entire domain appears to be largely homogeneous. When the aerosol injection rate is increased, domain-wide mixing becomes more inhomogeneous, which intensifies the local inhomogeneous mixing near the entrainment inlet. Even without entrainment, the near-wall regions with high variations in supersaturation can lead to a similar signature of inhomogeneous mixing caused by entrainment. Coarsening the grid spacing slightly reduces the evidence of local inhomogeneous mixing, yet the overall pattern across the domain aligns with that of a finer grid spacing. Last, variations in the entrainment velocity and temperature can shift the balance between droplet size and liquid water content,

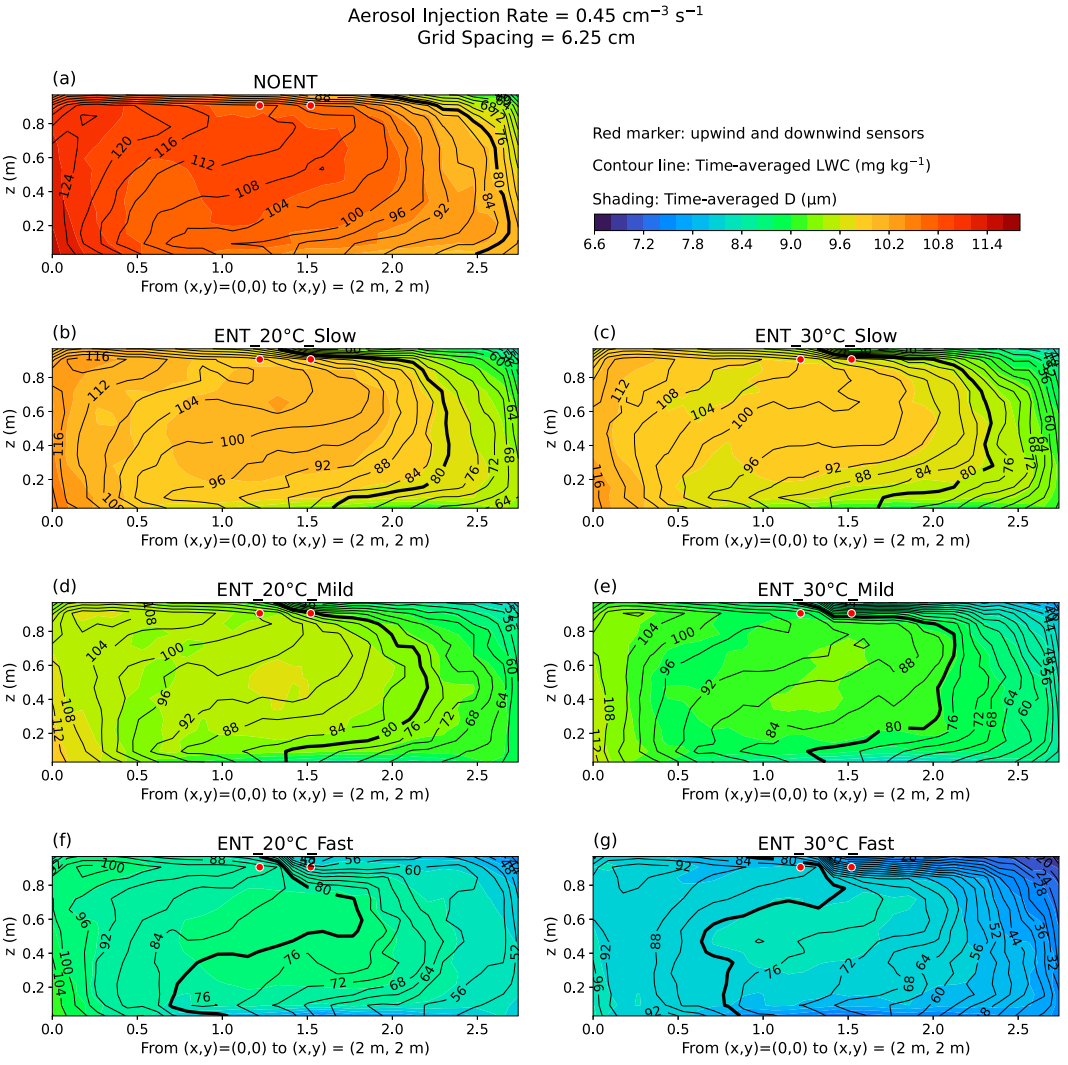

FIG. 11. As in Fig. 8, but for the simulations with a rougher grid spacing (6.25 cm).

signifying globally homogeneous mixing, which is consistent with the findings of Yeom et al. (2023). LESs further show that the heating and evaporation rates of the walls adjust in response to various entrainment velocities and temperatures, confirming that the globally homogeneous mixing signature results from comparing the microphysical properties in different equilibrium states, rather than from comparing the properties of an air mass immediately before and after entrainment.

These results can be interpreted in the context of the time scales identified in prior works, namely, the droplet evaporation time scale and the turbulent mixing time scale. An advantage of the experimental setup is that the scales for entrainment and the entire chamber are clearly defined, removing some of the ambiguity present in full-cloud measurements and simulations. Additionally, the work of Yeom et al. (2023) and that presented here suggest a shift in perspective from transient response to mixing to the comparison of steady states achieved from relaxation to steady entrainment with constant velocities and temperatures. This shift in perspective allows for the emergence of "locally inhomogeneous" versus "globally homogeneous" perspectives. Comparing steady states is a different assessment to the problem compared to the traditional focus on the transient response part of the problem.

Although the qualitative observations made using LES are reasonable and align with the results of the Pi chamber experiments, it is essential to consider some uncertainties within this study. First, the depth of entrainment reached is approximately 8–15 cm from the top wall in LES, which is shallower than 25 cm observed in the Pi chamber. This discrepancy could be attributed to the overestimation of diffusion in LES and the adverse pressure gradient force under the pseudo inlet. The overestimated diffusion also implies that the inhomogeneous mixing signature may be underrepresented. Second, to orient the LSC, the overall turbulent kinetic energy is increased by approximately 17%. This increase in the resolved turbulent mixing might also reduce the turbulent mixing time compared to that in the Pi chamber. Third, the aerosols are injected homogeneously into the domain in the simulations,

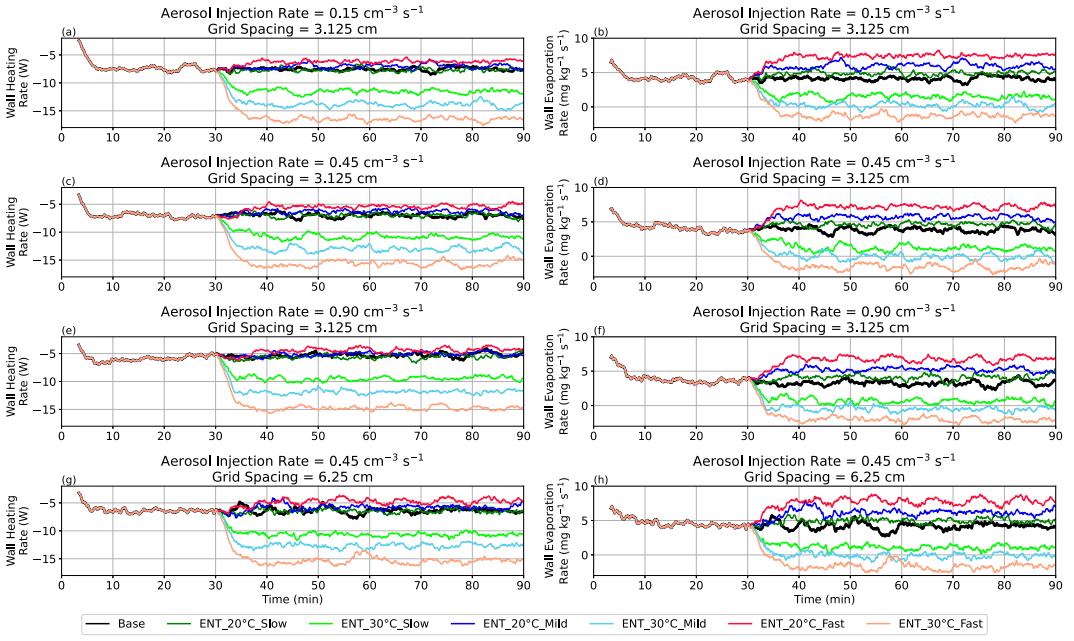

FIG. 12. The time series of (a),(c),(e),(g) wall heating and (b),(d),(f),(h) evaporation rates with a moving-average window of 200 s.

whereas they are injected from a single inlet in the real chamber. Thomas et al. (2023) have shown that the point injection of aerosols may broaden the resulting DSD, but this influence may be lessened with a higher aerosol injection rate. In the less polluted case, a broader DSD with increased droplet sizes may increase evaporation time and further enhance the inhomogeneous mixing signature. Last, while this study demonstrates that a combination of LES and bin microphysics can capture the signature of inhomogeneous mixing, it also reveals the sensitivity of these results to the grid spacing.

Finally, this work sheds light on the simulations and measurements of atmospheric clouds. The dependence of the inhomogeneous mixing signature on grid spacing implies that LESs of the atmospheric boundary layer may underestimate this mechanism. Specifically, if the entrained subsaturated air blob is larger than the LES grid spacing and the evaporation time is short enough, the blob can evaporate the droplet within the engulfed grid cells before mixing with the surrounding air parcels, thereby resolving the inhomogeneous mixing mechanism. However, blobs smaller than the grid spacing can only be addressed by appropriate SGS approaches. Additionally, the different wall fluxes causing the homogeneous mixing signature among various steady states confirm that the environment will respond according to the varying entrainment flux. This strengthens the connection to stratocumulus clouds with spatially varying entrainment velocities and temperatures at cloud top, as suggested by Yeom et al. (2023): an aircraft sampling at constant height will tend to observe a signature of homogeneous mixing if averaged over many large eddies with varying entrainment fluxes.

Acknowledgments. We acknowledge the discussions and suggestions from Dr. Marat Khairoutdinov, Dr. Fabian Hoffmann, Dr. Prasanth Prabhakaran, and Dr. Xiangyu Li. A. Wang and M. Ovchinnikov are supported by the U.S. Department of Energy (DOE) Office of Science Atmospheric System Research (ASR) project at PNNL. PNNL is operated for the DOE by Battelle Memorial Institute under Contract DE-AC05-76 RL01830. F. Yang was supported by the Office of Biological and Environmental Research in the DOE, Office of Science, through the DOE Contract DE-SC0012704 to Brookhaven National Laboratory. W. Cantrell, J. Yeom, and R. Shaw are supported by DOE ASR under Contract DE-SC0022128. This research used resources of the National Energy Research Scientific Computing Center (NERSC), a DOE Office of Science User Facility located at Lawrence Berkeley National Laboratory, operated under Contract No. DE-AC02-05CH11231 using NERSC Awards BER-ERCAP0024023 and BER-ERCAP0027865. Last, for transparency and following the position statement of the Committee on Publication Ethics (COPE), we acknowledge the assistance of ChatGPT in generating the first draft of data processing code, checking spelling, correcting grammar, along with some refinements for context, and providing some initial ideas for the introduction section.

Data availability statement. The SAM model was kindly provided by Dr. Marat Khairoutdinov and is publicly available at http://rossby.msrc.sunysb.edu/~marat/SAM.html. The output from the SAM simulations is stored on the NERSC HPSS storage system at https://portal.nersc.gov/archive/home/w/wang1202/www/Wang2024JAS_Entrainment/.

APPENDIX A

Measurement of Entrainment Depth via Temperature Fluctuation

To examine how far into the chamber the entrained air can penetrate, we place two virtual sensors. The horizontal locations of the two sensors are each 15 cm from the inlet center, one in the upwind and the other in the downwind regions. We vary the heights of the virtual sensors to detect entrainment signals, represented by the first to fourth columns in Fig. A1. The signals appear differently in different cases. Figures A1a–d show that, without entrainment (i.e., case NOENT), the temperature statistics are affected by the top cold wall, revealed by the left tail of the histograms. As the air parcel moves from the upwind to the downwind regions, the mixing with the cold air contacting the top wall increases, so the distribution in the downwind region slightly shifts to the left. When the entrainment air has the temperature of the average of the top and bottom walls (cases ENT_20°C_…; Figs. A1e–p,), the temperature is closer to 20°C in the downwind region. When the entrainment air is warmer than the domain (case ENT_30°C_…; Figs. A1q–ab), the temperature in the downwind region is higher than in the upwind region.

Regarding the depths at which the entrained air can reach, when the entrainment temperature is 20°C, the entrainment signal is slightly detectable at roughly 14 cm from the top (cf. Figs. A1h, l, p to d). When the entrainment temperature is 30°C, the influence of entrained air is detectable down to approximately 8, 11, and 14 cm from the top (Figs. A1r, w, ab), reaching shallower depths compared to the 20°C cases owing to stronger buoyancy effects. However, these depths are all shallower than the 25-cm depth detected in the real Pi chamber. This discrepancy may be attributed to the entrainment resistance caused by the pressure gradient force, or to the LES schemes that might overestimate the diffusion, like SGS models and advection schemes (e.g., Bou-Zeid et al. 2005; Wang et al. 2021).

In an effort to identify potential reasons for these discrepancies, we conduct an additional dry simulation, guided by the settings outlined in the supporting information of Yeom et al. (2023). Specifically, the temperatures are set to 20°, 25°, and 30°C for the top, side, and bottom walls, respectively, with all walls kept dry. The entrained dry air is maintained at 40°C with a mild velocity. The sensors in the upwind and downwind regions are each positioned 8 cm from the center of the inlet. The result of this simulation is presented in Fig. A2. The entrainment reaches roughly 10 cm from the top wall, still shallower than 15-cm depth detected by Yeom et al. (2023) for the dry experiment.

To further explore the reason for the shallower penetration of entrainment, we only examine the upwind region, where the numerical schemes can influence but the pressure gradient resistance does not affect. In the dry experiment conducted in the Pi chamber, as indicated in the supporting information of Yeom et al. (2023), the temperature fluctuation in the upwind region can reach approximately 23°C at $z = 85$ cm (see Fig. S1 in Yeom et al. 2023), whereas our LES model only shows a decrease to just below 24°C at $z = 89$ cm (Fig. A2c). Although this cannot exclude the influence of the adverse pressure gradient force, this confirms the overestimation of diffusion from the numerical schemes in LES.

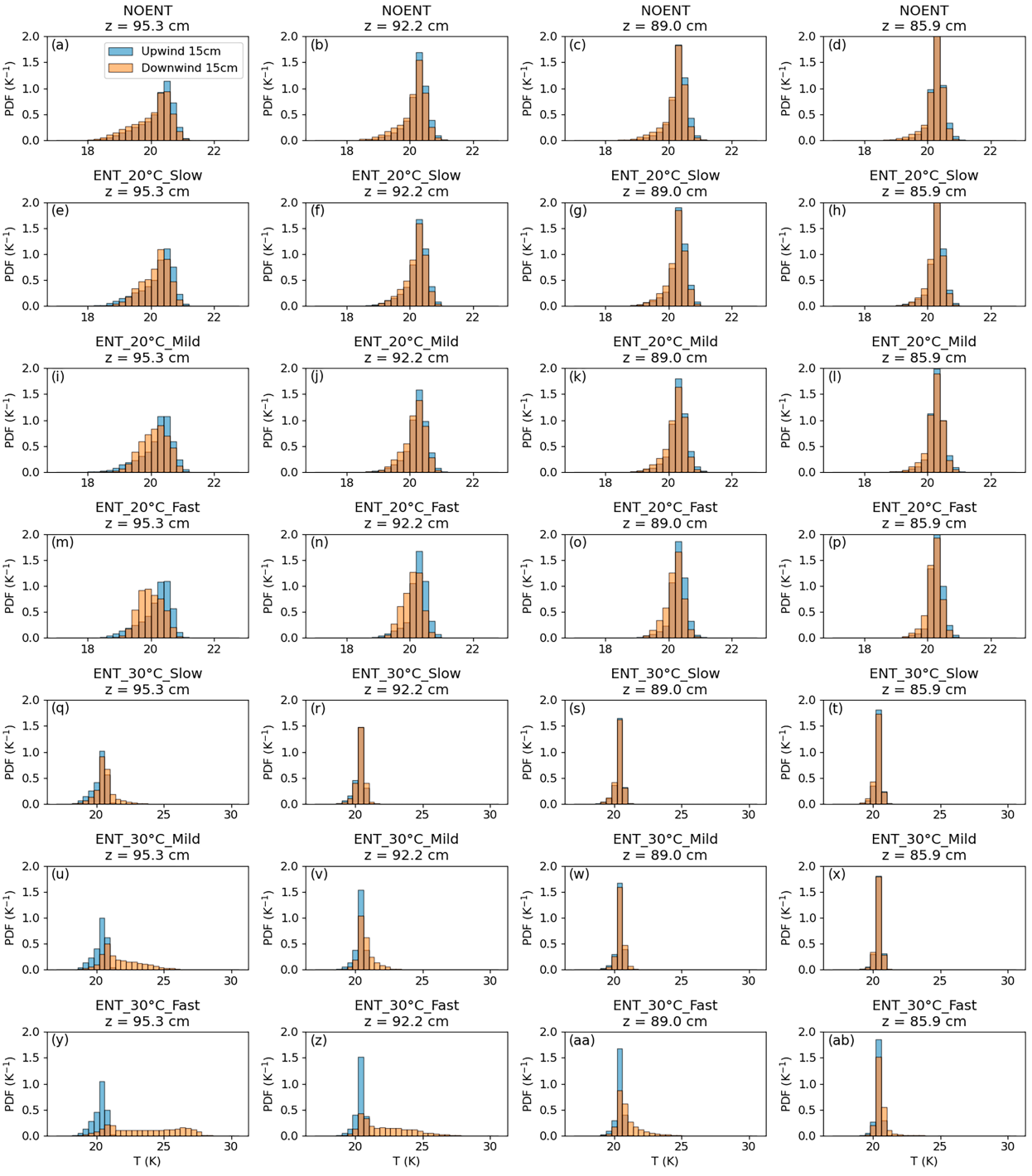

FIG. A1. Temperature fluctuations at upwind (blue) and downwind (orange) regions at (from left to right) four different heights and (from top to bottom) seven cases. The statistics were derived from time series data collected between t = 60–90 min by virtual sensors set in the simulation to record the temperature at each time step.

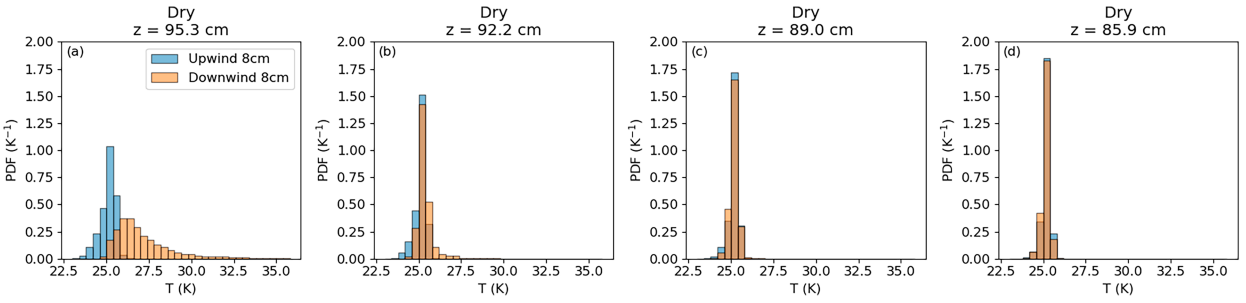

FIG. A2. As in Fig. A1, but for the dry simulation to be compared with that in the Fig. S1 in the supporting information of Yeom et al. (2023).

APPENDIX B

The Droplet Size Distributions for Other Conditions

Figures B1–B3 serve as an extension of section 3c to present the DSDs for the three remaining conditions not displayed in Fig. 5.

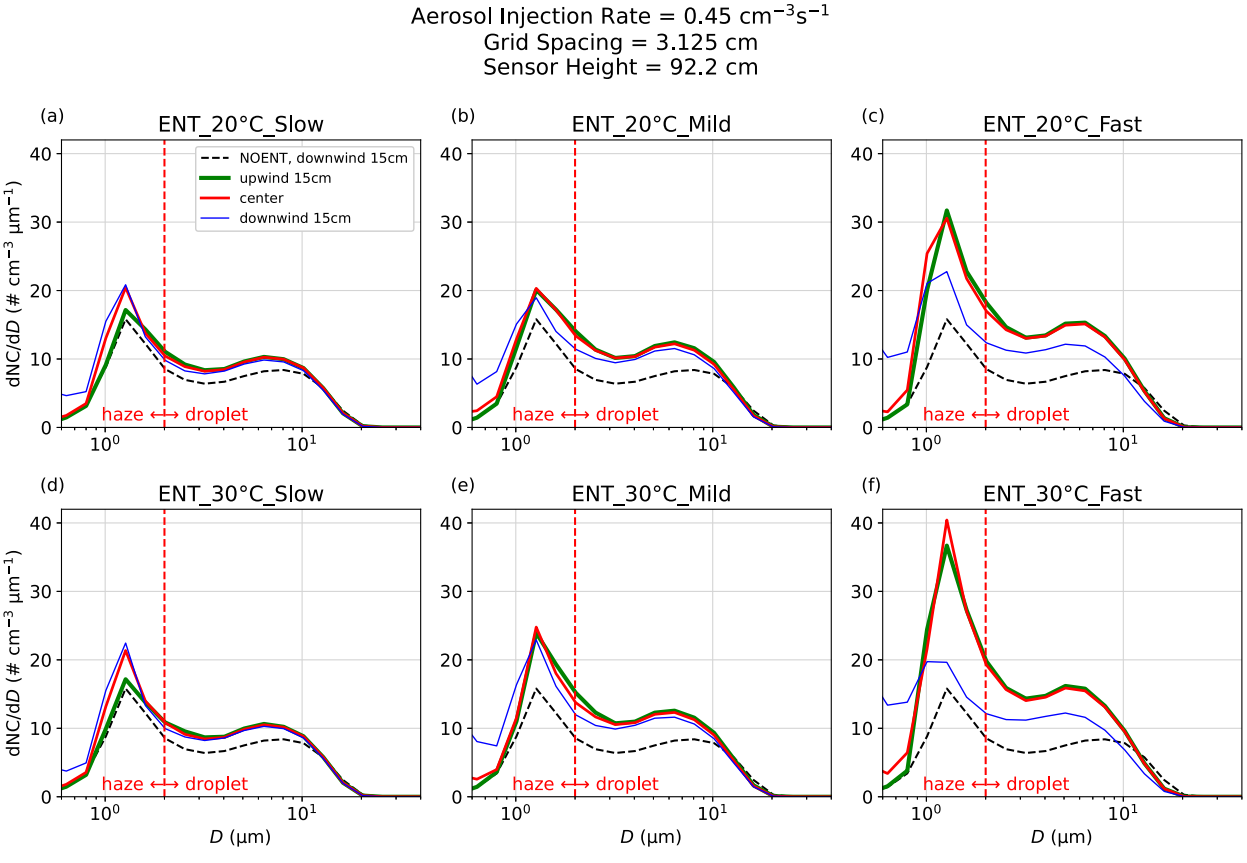

FIG. B1. As in Fig. 5, but for the conditions of the aerosol injection rate = 0.45 cm^{-3} s^{-1} and grid spacing = 3.125 cm.

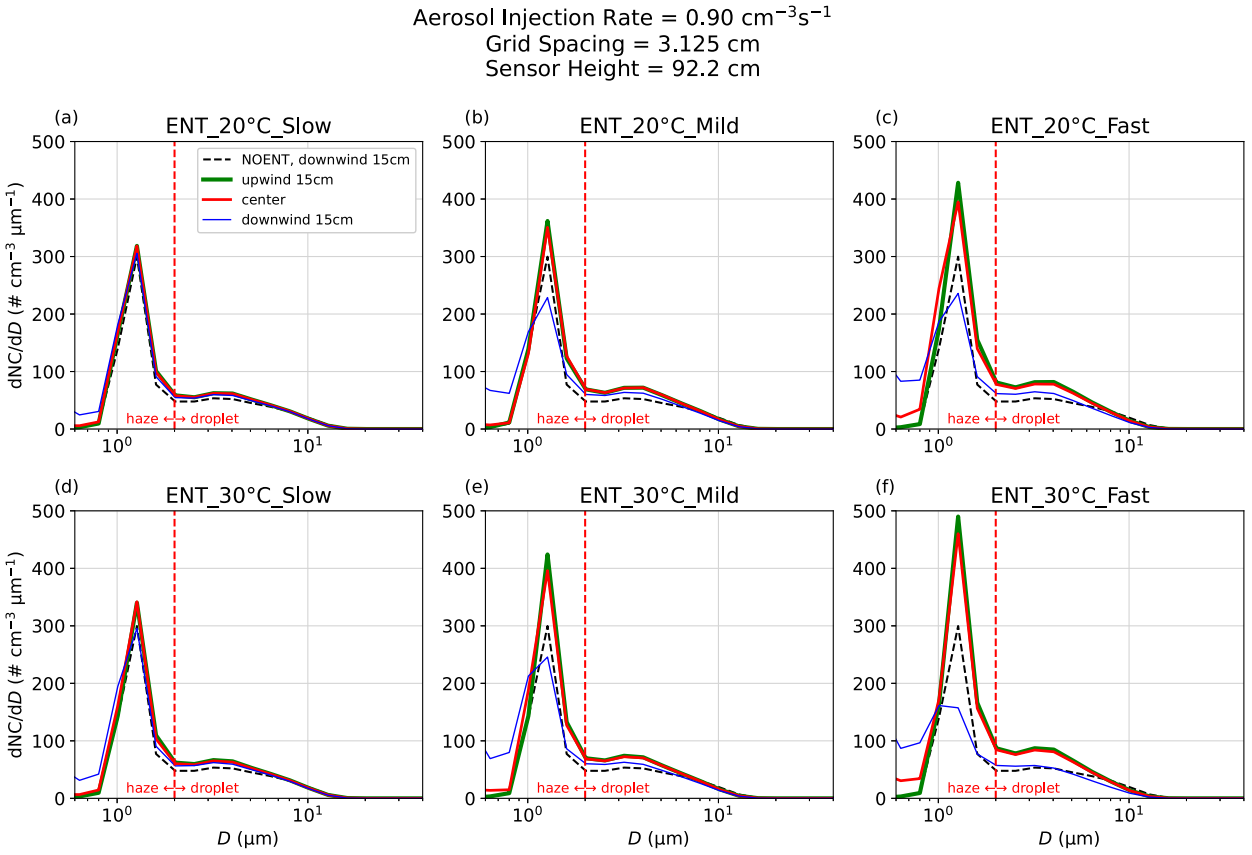

FIG. B2. As in Fig. 5, but for the conditions of the aerosol injection rate = 0.90 cm^{-3} s^{-1} and grid spacing = 3.125 cm.

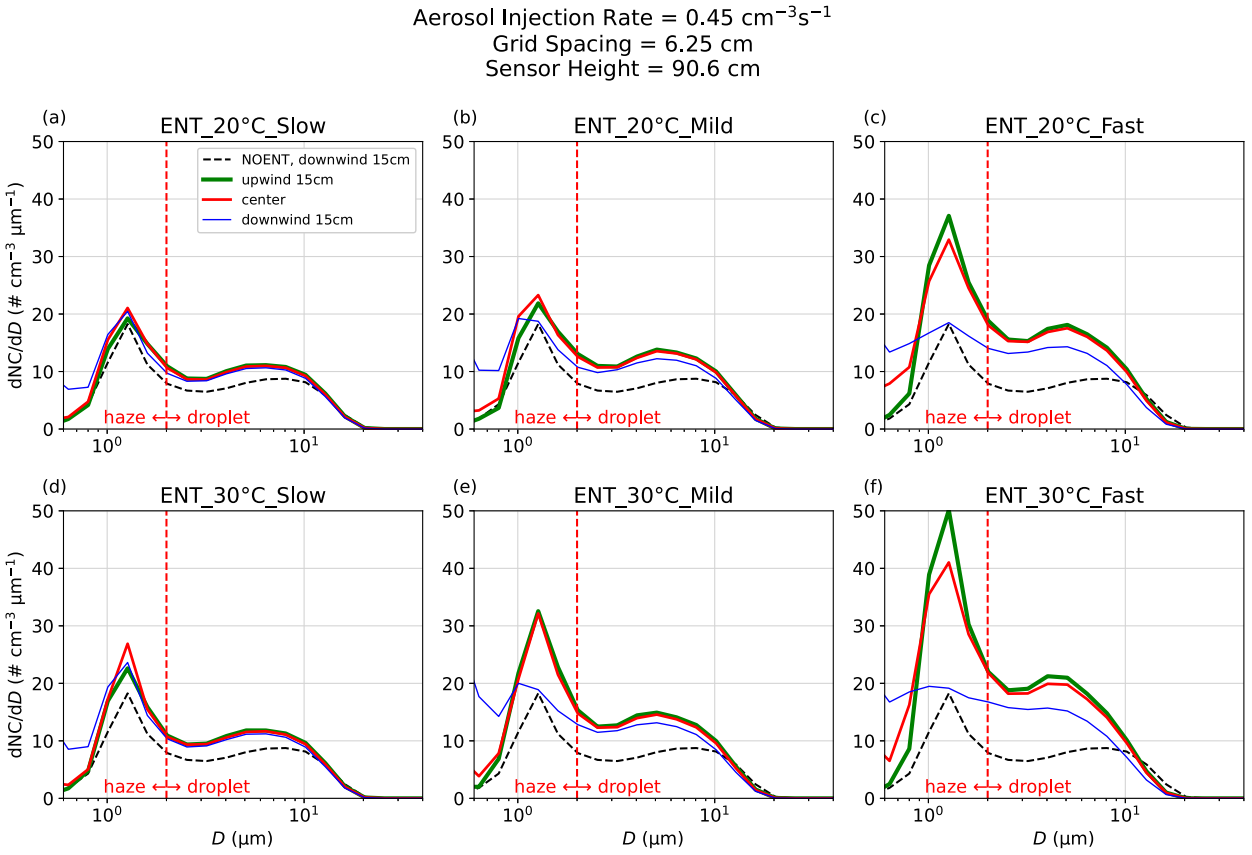

FIG. B3. As in Fig. 5, but for the conditions of the aerosol injection rate = 0.45 cm^{-3} s^{-1} and grid spacing = 6.25 cm.

APPENDIX C

The Higher RH near the Lower Surface Revealed by DNS

From the supersaturation distribution revealed in Fig. 10, an extended question is as follows: Why does the updraft contain higher supersaturation than the downdraft, even without entrainment? Upon mixing with the air from the interior of the domain, the supersaturation near the bottom increases because of the high moisture, and the supersaturation increases near the top because of the low temperature. However, the diffusivity for moisture is higher than the diffusivity for temperature (i.e., Prandtl number is lower than Schmidt number; e.g., Hickey et al. 2000), causing the supersaturation near the bottom to exceed that near the top. When the higher diffusivity for moisture is considered in the wall model, the roughness length for moisture is higher than that for temperature (Brutsaert 1982; Garratt 1994; Wang et al. 2024b).

To confirm this reasoning, we perform an additional moist DNS without microphysics. Following Wang et al. (2024c), we use SAM to perform DNS by replacing the SGS model with molecular viscosity and the wall model with explicit molecular dissipation. The Prandtl number is 0.72 and the Schmidt number is 0.62, the same as those used in Chandrakar et al. (2022). The domain is 1 m × 1 m × 1 m with uniform 512 grid cells in each direction, resulting in a uniform grid spacing of ~2 mm, same as Wang et al. (2024c). However, unlike Wang et al. (2024c), here the sidewalls are solid and no penetration. The temperatures for the top, bottom, and sidewalls are 282, 294, and 288 K, respectively. All walls are saturated. The simulation is performed for 10 min, reaching the steady state within 2 min. To exclude any other artificial influence, we do not apply the pseudo inlet and LSC forcing for the DNS.

A snapshot of the supersaturation field is presented in Fig. C1. The result shows that, even without entrainment, cloud microphysics, and wall models, the supersaturation near the bottom is higher than that near the top. Specifically, the supersaturation adjacent to the bottom is nearly zero before the air mixes with the environment. After mixing with air from the interior of the domain, the supersaturation increases and reaches its maximum at the edges of the plumes near the bottom because of the more efficient diffusion of high moisture than high temperature. With further mixing with the ambient air, the moisture and temperature (and thus the supersaturation) approach the domain-average values.

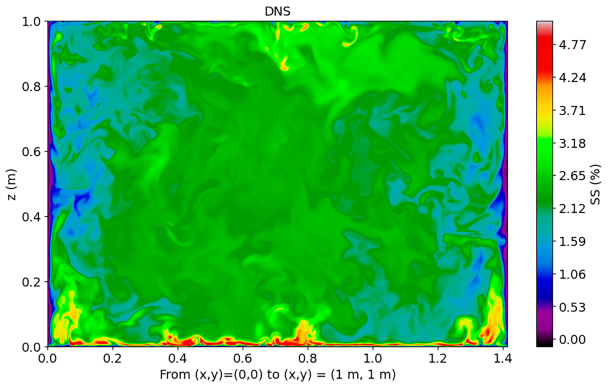

FIG. C1. A diagonal slice of the supersaturation field in the moist DNS at $t = 7$ min.

REFERENCES

Abma, D., T. Heus, and J. P. Mellado, 2013: Direct numerical simulation of evaporative cooling at the lateral boundary of shallow cumulus clouds. *J. Atmos. Sci.*, **70**, 2088–2102, https://doi.org/10.1175/JAS-D-12-0230.1.

Ahlers, G., S. Grossmann, and D. Lohse, 2009: Heat transfer and large scale dynamics in turbulent Rayleigh-Bénard convection. *Rev. Mod. Phys.*, **81**, 503–537, https://doi.org/10.1103/RevModPhys.81.503.

Anderson, J. C., S. Thomas, P. Prabhakaran, R. A. Shaw, and W. Cantrell, 2021: Effects of the large-scale circulation on temperature and water vapor distributions in the π Chamber. *Atmos. Meas. Tech.*, **14**, 5473–5485, https://doi.org/10.5194/amt-14-5473-2021.

Baker, M. B., R. Corbin, and J. Latham, 1980: The influence of entrainment on the evolution of cloud droplet spectra: I. A model of inhomogeneous mixing. *Quart. J. Roy. Meteor. Soc.*, **106**, 581–598, https://doi.org/10.1002/qj.49710644914.

Beals, M. A., J. P. Fugal, R. A. Shaw, J. Lu, S. M. Spuler, and J. L. Stith, 2015: Holographic measurements of inhomogeneous cloud mixing at the centimeter scale. *Science*, **350**, 87–90, https://doi.org/10.1126/science.aab0751.

Bou-Zeid, E., C. Meneveau, and M. B. Parlange, 2005: A scale-dependent Lagrangian dynamic model for large eddy simulation of complex turbulent flows. *Phys. Fluids*, **17**, 025105, https://doi.org/10.1063/1.1839152.

Brutsaert, W., 1982: *Evaporation into the Atmosphere: Theory, History and Applications*. Environmental Fluid Mechanics, Vol. 1, Springer, 302 pp., https://doi.org/10.1007/978-94-017-1497-6.

Chandrakar, K. K., W. Cantrell, K. Chang, D. Ciochetto, D. Niedermeier, M. Ovchinnikov, R. A. Shaw, and F. Yang, 2016: Aerosol indirect effect from turbulence-induced broadening of cloud-droplet size distributions. *Proc. Natl. Acad. Sci. USA*, **113**, 14 243–14 248, https://doi.org/10.1073/pnas.1612686113.

——, H. Morrison, W. W. Grabowski, G. H. Bryan, and R. A. Shaw, 2022: Supersaturation variability from scalar mixing: Evaluation of a new subgrid-scale model using direct numerical simulations of turbulent Rayleigh–Bénard convection. *J. Atmos. Sci.*, **79**, 1191–1210, https://doi.org/10.1175/JAS-D-21-0250.1.

——, ——, and R. A. Shaw, 2023: Lagrangian and Eulerian supersaturation statistics in turbulent cloudy Rayleigh–Bénard convection: Applications for LES subgrid modeling. *J. Atmos. Sci.*, **80**, 2261–2285, https://doi.org/10.1175/JAS-D-22-0256.1.

Chang, K., and Coauthors, 2016: A laboratory facility to study gas–aerosol–cloud interactions in a turbulent environment: The π chamber. *Bull. Amer. Meteor. Soc.*, **97**, 2343–2358, https://doi.org/10.1175/BAMS-D-15-00203.1.

Chen, J.-P., and D. Lamb, 1994: Simulation of cloud microphysical and chemical processes using a multicomponent framework. Part I: Description of the microphysical model. *J. Atmos. Sci.*, **51**, 2613–2630, https://doi.org/10.1175/1520-0469(1994)051<2613:SOCMAC>2.0.CO;2.

Desai, N., Y. Liu, S. Glienke, R. A. Shaw, C. Lu, J. Wang, and S. Gao, 2021: Vertical variation of turbulent entrainment mixing processes in marine stratocumulus clouds using high-resolution digital holography. *J. Geophys. Res. Atmos.*, **126**, e2020JD033527, https://doi.org/10.1029/2020JD033527.

Driedonks, A. G. M., and P. G. Duynkerke, 1989: Current problems in the stratocumulus-topped atmospheric boundary layer. *Bound.-Layer Meteor.*, **46**, 275–303, https://doi.org/10.1007/BF00120843.

Garratt, J. R., 1994: *The Atmospheric Boundary Layer*. Cambridge University Press, 316 pp.

Ghonima, M. S., T. Heus, J. R. Norris, and J. Kleissl, 2016: Factors controlling stratocumulus cloud lifetime over coastal land. *J. Atmos. Sci.*, **73**, 2961–2983, https://doi.org/10.1175/JAS-D-15-0228.1.

Grabowski, W. W., 2020: Comparison of Eulerian bin and Lagrangian particle-based schemes in simulations of Pi Chamber dynamics and microphysics. *J. Atmos. Sci.*, **77**, 1151–1165, https://doi.org/10.1175/JAS-D-19-0216.1.

——, H. Morrison, S.-I. Shima, G. C. Abade, P. Dziekan, and H. Pawlowska, 2019: Modeling of cloud microphysics: Can we do better? *Bull. Amer. Meteor. Soc.*, **100**, 655–672, https://doi.org/10.1175/BAMS-D-18-0005.1.

Haman, K. E., S. P. Malinowski, M. J. Kurowski, H. Gerber, and J. Brenguier, 2007: Small scale mixing processes at the top of a marine stratocumulus—a case study. *Quart. J. Roy. Meteor. Soc.*, **133**, 213–226, https://doi.org/10.1002/qj.5.

Hickey, C. J., R. Raspet, and W. V. Slaton, 2000: Effects of thermal diffusion on sound attenuation in evaporating and condensing gas-vapor mixtures in tubes. *J. Acoust. Soc. Amer.*, **107**, 1126–1130, https://doi.org/10.1121/1.428403.

Hoffmann, F., T. Yamaguchi, and G. Feingold, 2019: Inhomogeneous mixing in Lagrangian cloud models: Effects on the production of precipitation embryos. *J. Atmos. Sci.*, **76**, 113–133, https://doi.org/10.1175/JAS-D-18-0087.1.

Huang, J. M., and J. Zhang, 2023: Rayleigh–Bénard thermal convection perturbed by a horizontal heat flux. *J. Fluid Mech.*, **954**, R2, https://doi.org/10.1017/jfm.2022.1035.

Jensen, J. B., P. H. Austin, M. B. Baker, and A. M. Blyth, 1985: Turbulent mixing, spectral evolution and dynamics in a warm cumulus cloud. *J. Atmos. Sci.*, **42**, 173–192, https://doi.org/10.1175/1520-0469(1985)042<0173:TMSEAD>2.0.CO;2.

Jiang, H., H. Xue, A. Teller, G. Feingold, and Z. Levin, 2006: Aerosol effects on the lifetime of shallow cumulus. *Geophys. Res. Lett.*, **33**, L14806, https://doi.org/10.1029/2006GL026024.

Kays, W. M., M. E. Crawford, and B. Weigand, 1980: *Convective Heat and Mass Transfer*. 4th ed. McGraw-Hill, 347 pp.

Khairoutdinov, M. F., and D. A. Randall, 2003: Cloud resolving modeling of the arm summer 1997 IOP: Model formulation, results, uncertainties, and sensitivities. *J. Atmos. Sci.*, **60**, 607–625, https://doi.org/10.1175/1520-0469(2003)060<0607:CRMOTA>2.0.CO;2.

Kumar, B., J. Schumacher, and R. A. Shaw, 2013: Cloud microphysical effects of turbulent mixing and entrainment. *Theor. Comput. Fluid Dyn.*, **27**, 361–376, https://doi.org/10.1007/s00162-012-0272-z.

——, ——, and ——, 2014: Lagrangian mixing dynamics at the cloudy–clear air interface. *J. Atmos. Sci.*, **71**, 2564–2580, https://doi.org/10.1175/JAS-D-13-0294.1.

——, P. Götzfried, N. Suresh, J. Schumacher, and R. A. Shaw, 2018: Scale dependence of cloud microphysical response to turbulent entrainment and mixing. *J. Adv. Model. Earth Syst.*, **10**, 2777–2785, https://doi.org/10.1029/2018MS001487.

Latham, J., and R. L. Reed, 1977: Laboratory studies of the effects of mixing on the evolution of cloud droplet spectra. *Quart. J. Roy. Meteor. Soc.*, **103**, 297–306, https://doi.org/10.1002/qj.49710343607.

Lehmann, K., H. Siebert, and R. A. Shaw, 2009: Homogeneous and inhomogeneous mixing in cumulus clouds: Dependence on local turbulence structure. *J. Atmos. Sci.*, **66**, 3641–3659, https://doi.org/10.1175/2009JAS3012.1.

Lilly, D. K., 1968: Models of cloud-topped mixed layers under a strong inversion. *Quart. J. Roy. Meteor. Soc.*, **94**, 292–309, https://doi.org/10.1002/qj.49709440106.

Lu, C., Y. Liu, and S. Niu, 2011: Examination of turbulent entrainment-mixing mechanisms using a combined approach. *J. Geophys. Res.*, **116**, D20207, https://doi.org/10.1029/2011JD015944.

——, and Coauthors, 2023: Observational study of relationships between entrainment rate, homogeneity of mixing, and cloud droplet relative dispersion. *Atmos. Res.*, **293**, 106900, https://doi.org/10.1016/j.atmosres.2023.106900.

MacMillan, T., R. A. Shaw, W. H. Cantrell, and D. H. Richter, 2022: Direct numerical simulation of turbulence and microphysics in the Pi chamber. *Phys. Rev. Fluids*, **7**, 020501, https://doi.org/10.1103/PhysRevFluids.7.020501.

Mason, B. J., and P. R. Jonas, 1974: The evolution of droplet spectra and large droplets by condensation in cumulus clouds. *Quart. J. Roy. Meteor. Soc.*, **100**, 23–38, https://doi.org/10.1002/qj.49710042304.

Monin, A. S., and A. M. Obukhov, 1954: Basic laws of turbulent mixing in the atmosphere near the ground. *Tr. Geofiz. Inst., Akad. Nauk SSSR*, **24**, 163–187.

Morrison, H., M. Witte, G. H. Bryan, J. Y. Harrington, and Z. J. Lebo, 2018: Broadening of modeled cloud droplet spectra using bin microphysics in an Eulerian spatial domain. *J. Atmos. Sci.*, **75**, 4005–4030, https://doi.org/10.1175/JAS-D-18-0055.1.

Smolarkiewicz, P. K., and W. W. Grabowski, 1990: The multidimensional positive definite advection transport algorithm: Nonoscillatory option. *J. Comput. Phys.*, **86**, 355–375, https://doi.org/10.1016/0021-9991(90)90105-A.

Stevens, B., 2002: Entrainment in stratocumulus-topped mixed layers. *Quart. J. Roy. Meteor. Soc.*, **128**, 2663–2690, https://doi.org/10.1256/qj.01.202.

Thomas, S., M. Ovchinnikov, F. Yang, D. van der Voort, W. Cantrell, S. K. Krueger, and R. A. Shaw, 2019: Scaling of an atmospheric model to simulate turbulence and cloud microphysics in the Pi Chamber. *J. Adv. Model. Earth Syst.*, **11**, 1981–1994, https://doi.org/10.1029/2019MS001670.

——, F. Yang, M. Ovchinnikov, W. H. Cantrell, and R. A. Shaw, 2023: Scaling of turbulence and microphysics in a convection–cloud chamber of varying height. *J. Adv. Model. Earth Syst.*, **15**, e2022MS003304, https://doi.org/10.1029/2022MS003304.

Tölle, M. H., and S. K. Krueger, 2014: Effects of entrainment and mixing on droplet size distributions in warm cumulus clouds. *J. Adv. Model. Earth Syst.*, **6**, 281–299, https://doi.org/10.1002/2012MS000209.

Wang, A., Y. Pan, and P. M. Markowski, 2021: The influence of WENO schemes on large-eddy simulations of a neutral atmospheric boundary layer. *J. Atmos. Sci.*, **78**, 3613–3628, https://doi.org/10.1175/JAS-D-21-0033.1.

——, ——, G. H. Bryan, and P. M. Markowski, 2023: Modeling near-surface turbulence in large-eddy simulations of a tornado: An application of thin boundary layer equations. *Mon. Wea. Rev.*, **151**, 1587–1607, https://doi.org/10.1175/MWR-D-22-0060.1.

——, S. Krueger, S. Chen, M. Ovchinnikov, W. Cantrell, and R. A. Shaw, 2024a: Glaciation of mixed-phase clouds: Insights from bulk model and bin-microphysics large-eddy simulation informed by laboratory experiment. *Atmos. Chem. Phys.*, **24**, 10 245–10 260, https://doi.org/10.5194/acp-24-10245-2024.

——, M. Ovchinnikov, F. Yang, S. Schmalfuss, and R. A. Shaw, 2024b: Designing a convection-cloud chamber for collision-coalescence using large-eddy simulation with bin microphysics. *J. Adv. Model. Earth Syst.*, **16**, e2023MS003734, https://doi.org/10.1029/2023MS003734.

——, X. I. A. Yang, and M. Ovchinnikov, 2024c: An investigation of LES wall modeling for Rayleigh–Bénard convection via interpretable and physics-aware feedforward neural networks with DNS. *J. Atmos. Sci.*, **81**, 435–458, https://doi.org/10.1175/JAS-D-23-0094.1.

Wang, J., P. H. Daum, S. S. Yum, Y. Liu, G. I. Senum, M.-L. Lu, J. H. Seinfeld, and H. Jonsson, 2009: Observations of marine stratocumulus microphysics and implications for processes controlling droplet spectra: Results from the Marine Stratus/Stratocumulus Experiment. *J. Geophys. Res.*, **114**, D18210, https://doi.org/10.1029/2008JD011035.

Warner, J., 1973: The microstructure of cumulus cloud: Part IV. The effect on the droplet spectrum of mixing between cloud and environment. *J. Atmos. Sci.*, **30**, 256–261, https://doi.org/10.1175/1520-0469(1973)030<0256:TMOCCP>2.0.CO;2.

Wood, R., 2012: Stratocumulus clouds. *Mon. Wea. Rev.*, **140**, 2373–2423, https://doi.org/10.1175/MWR-D-11-00121.1.

Yang, F., M. Ovchinnikov, S. Thomas, A. Khain, R. McGraw, R. A. Shaw, and A. M. Vogelmann, 2022: Large-eddy simulations of a convection cloud chamber: Sensitivity to bin microphysics and advection. *J. Adv. Model. Earth Syst.*, **14**, e2021MS002895, https://doi.org/10.1029/2021MS002895.

——, F. Hoffmann, R. A. Shaw, M. Ovchinnikov, and A. M. Vogelmann, 2023: An intercomparison of large-eddy simulations of a convection cloud chamber using haze-capable bin and Lagrangian cloud microphysics schemes. *J. Adv. Model. Earth Syst.*, **15**, e2022MS003270, https://doi.org/10.1029/2022MS003270.

——, H. F. Sadi, R. A. Shaw, F. Hoffmann, P. Hou, A. Wang, and M. Ovchinnikov, 2024: Microphysics regimes due to haze-cloud interactions: Cloud oscillation and cloud collapse, *EGUsphere*, https://doi.org/10.5194/egusphere-2024-1693.

Yau, M. K., and R. R. Rogers, 1996: *A Short Course in Cloud Physics*. Elsevier, 304 pp.

Yeom, J. M., S. S. Yum, Y. Liu, and C. Lu, 2017: A study on the entrainment and mixing process in the continental stratocumulus clouds measured during the RACORO campaign. *Atmos. Res.*, **194**, 89–99, https://doi.org/10.1016/j.atmosres.2017.04.028.

——, and Coauthors, 2021: Vertical variations of cloud microphysical relationships in marine stratocumulus clouds observed during the ACE-ENA campaign. *J. Geophys. Res.*

Atmos., **126**, e2021JD034700, https://doi.org/10.1029/2021JD034700.

——, I. Helman, P. Prabhakaran, J. C. Anderson, F. Yang, R. A. Shaw, and W. Cantrell, 2023: Cloud microphysical response to entrainment and mixing is locally inhomogeneous and globally homogeneous: Evidence from the lab. *Proc. Natl. Acad. Sci. USA*, **120**, e2307354120, https://doi.org/10.1073/pnas.2307354120.

——, K.-E. Szodry, H. Siebert, A. Ehrlich, J. P. Mellado, R. A. Shaw, and S. S. Yum, 2024: High-resolution measurements of microphysics and entrainment in marine stratocumulus clouds. *Quart. J. Roy. Meteor. Soc.*, **150**, 81–97, https://doi.org/10.1002/qj.4586.

Yum, S. S., J. Wang, Y. Liu, G. Senum, S. Springston, R. McGraw, and J. M. Yeom, 2015: Cloud microphysical relationships and their implication on entrainment and mixing mechanism for the stratocumulus clouds measured during the VOCALS project. *J. Geophys. Res. Atmos.*, **120**, 5047–5069, https://doi.org/10.1002/2014JD022802.